





## Article

# Crystallization Sequence of the Spodumene-Rich Alijó Pegmatite (Northern Portugal) and Related Metasomatism on Its Host Rock

Idoia Garate-Olave <sup>1,\*</sup>, Encarnación Roda-Robles <sup>1</sup>, Nora Santos-Loyola <sup>1</sup>, Tania Martins <sup>2</sup>, Alexandre Lima <sup>3,4</sup>  
and Jon Errandonea-Martin <sup>1</sup>

<sup>1</sup> Geology Department, University of the Basque Country (UPV/EHU), Sarriena Street n/n, 48940 Leioa, Spain; encar.roda@ehu.eus (E.R.-R.); nora.santos@ehu.eus (N.S.-L.); jon.errandonea@ehu.eus (J.E.-M.)

<sup>2</sup> Manitoba Geological Survey, 360-1395 Ellice Avenue, Winnipeg, MB R3G 3P2, Canada; tania.martins@gov.mb.ca

<sup>3</sup> Department of Geosciences, Environment and Spatial Planning, Faculty of Sciences, University of Porto, Rua Campo Alegre, 4169-007 Porto, Portugal; allima@fc.up.pt

<sup>4</sup> ICT (Institute of Earth Sciences), Porto Pole, Rua Campo Alegre, 4169-007 Porto, Portugal

\* Correspondence: idoia.garate@ehu.eus

**Abstract:** The Barroso–Alvão region is an excellent setting for studying Li mineralization associated with granitic pegmatites and developing Li exploration techniques. Among the distinguished pegmatite types in this pegmatite field, the spodumene-bearing dyke from Alijó is a representative example of an Iberian Li–Cs–Ta (LCT) pegmatite currently under exploitation. In this work, we examine the internal evolution of the Alijó dyke and its external metasomatic effect on the surrounding metasediments, contributing to lithium exploration techniques. Electron microprobe analyses provided clues about the crystallization conditions and the degree of differentiation of the pegmatitic melt, whereas the external metasomatism induced by the spodumene-bearing pegmatite was studied through whole-rock geochemistry. The obtained results indicate that the primary crystallization of the studied dyke likely occurred at temperatures between 450–500 °C, with emplacement at shallow crustal levels of about 2–3 kbar. The high concentrations of trace elements such as Li, Cs, Rb, Be, Sn, Nb, Ta, Ge, U, and Tl in the pegmatitic melt suggests high availability of these elements, allowing their partitioning into an early exsolved fluid phase. The exsolution of this fluid phase, subtracting components such as F and B, from the pegmatitic melt would cause a significant undercooling of the melt. Moreover, the interaction of this expelled fluid with the country rock generated a metasomatic overprint in the surrounding metasedimentary host rocks. The metasomatic effect in Alijó is strongly influenced by the nature of the host metasediments, with a significantly higher grade of metasomatism observed in pelitic (mica-rich) samples compared to psammitic (mica-poor) samples collected at same distances from the dyke. The greisen developed close to the pegmatite contact reflects this metasomatic signature, characterized by the mobilization of at least B, F, Li, Rb, Cs, Sn, Be, Nb, Ta, and Tl. We cautiously suggest that whole rock Li concentrations greater than 300 ppm, combined with a minimum value of 1000 ppm for the sum of B, F, Li, Rb, Cs, and Sn in pelitic metasediments of Barroso–Alvão, may be indicative of a mineralized pegmatite in this region.

**Keywords:** spodumene; pegmatite; lithium exploration; metasomatism; Barroso–Alvão; Iberian Massif



**Citation:** Garate-Olave, I.; Roda-Robles, E.; Santos-Loyola, N.; Martins, T.; Lima, A.; Errandonea-Martin, J. Crystallization Sequence of the Spodumene-Rich Alijó Pegmatite (Northern Portugal) and Related Metasomatism on Its Host Rock. *Minerals* **2024**, *14*, 701. <https://doi.org/10.3390/min14070701>

Academic Editors: Zhenjiang Liu and Fangfang Zhang

Received: 4 June 2024

Revised: 5 July 2024

Accepted: 7 July 2024

Published: 9 July 2024



**Copyright:** © 2024 by the authors. Licensee MDPI, Basel, Switzerland. This article is an open access article distributed under the terms and conditions of the Creative Commons Attribution (CC BY) license (<https://creativecommons.org/licenses/by/4.0/>).

## 1. Introduction

Lithium demand as a high-technology metal has increased considerably in the last decades [1–3]. The use of this element in rechargeable batteries, high-capacity energy storage, and capacitors for wireless technology has made it a strategic metal for the current society [4–6]. As a logical consequence, scientific knowledge about the location of Li-bearing mineralization has become a priority for the European Union [7,8].

Among the different types of existing lithium mineralization, pegmatites are considered a feasible source of many critical raw materials [5,9]. Rare element pegmatites,

especially those included in the Li–Cs–Ta (LCT) family, show marked enrichment in a variety of chemical elements such as Li, Rb, Cs, Be, Sn, Ta, P, B, and F [10,11]. The chemical behavior of these incompatible elements in granite-pegmatite systems is of increasing interest among the scientific community. The distribution of incompatible elements in pegmatite-forming minerals during pegmatite crystallization has been proven to be an excellent tool for estimating the fractionation degree of a pegmatite body (e.g., [11,12]). As a result, the chemical variation in micas, quartz, and feldspars, among others, has become a principal objective in the exploration of pegmatite-related critical raw materials [8,13,14]. However, the magmatic–hydrothermal transition in pegmatitic systems is still a matter of debate, and the behavior of the aforementioned elements in the presence of coexisting fluids is not fully understood [15–18].

In this work, we present a mineralogical and whole-rock geochemical characterization of a spodumene-bearing pegmatite and its metasedimentary host rocks. This contribution provides new insights not only into the internal magmatic–hydrothermal evolution of this Li-bearing pegmatite but also into the metasomatic processes developed in the adjacent host rocks. The studied pegmatite, located in northern Portugal, is currently under exploitation and represents a good example of the late-Variscan LCT pegmatites that occur in NW Iberia, so its study would contribute to the understanding of the formation history of pegmatitic rocks. Moreover, the inferences about the geochemical halos generated around the studied pegmatite could be extended to other mineralized LCT pegmatites in the European Variscan Belt, providing new data to consider in less-invasive mineral exploration techniques.

## 2. Geological Setting

The Barroso–Alvão (BA) region is known for its vast Li mineralization associated with pegmatites (e.g., [19–21]). This prolific pegmatite field is located in northern Portugal, in the most westerly portion of the European Variscan Belt, the Iberian Massif (Figure 1). Of the several geotectonic zones that compose the Iberian Massif, the study area belongs to the Galicia-Trás-os-Montes Zone (GTMZ) as defined by [22], specifically to the Schistose Domain or Parautochthon, and is close to the basal thrust that represents the southern boundary with the Central Iberian Zone (CIZ) [22–24].

The Schistose Domain or Parautochthon comprises preorogenic Cambro–Silurian sedimentary successions and Devonian–Carboniferous synorogenic sequences, with minor Ordovician felsic volcanics [24,25]. This sedimentary record has been interpreted as distal deposits of the Gondwanan continental margin, showing affinities with the autochthonous CIZ (e.g., [24,26]). The main hosts for the pegmatites of the BA Pegmatite Field include mica schists, quartz-feldspathic schists, phyllites, quartz phyllites, quartzites, metagreywackes, cherts, and minor calcsilicate rocks [27].

The BA region was affected by three deformation phases of the Variscan Orogeny (D1 to D3) recognized by S1–S3 foliations, resulting in an imbricated internal structure [28–30]. Intermediate-pressure Barrovian metamorphism reached up to medium-grade conditions in the internal areas of the GTMZ [26], with pressure–temperature peak estimations for the BA region established at  $T = 500\text{--}550\text{ }^{\circ}\text{C}$  and  $P = \sim 3\text{ kbar}$ , within the amphibolite facies [30]. The studied areas belong to the biotite and andalusite zones, displaying isogrades with a general WNW–ESE direction, roughly parallel to the nearby Variscan granitoids located to the south of the pegmatite field [28,30] (Figure 1). Another remarkable structural feature of the area is its proximity to the Regua-Verin fault, one of the major sets of NNE–SSW faults in the region.

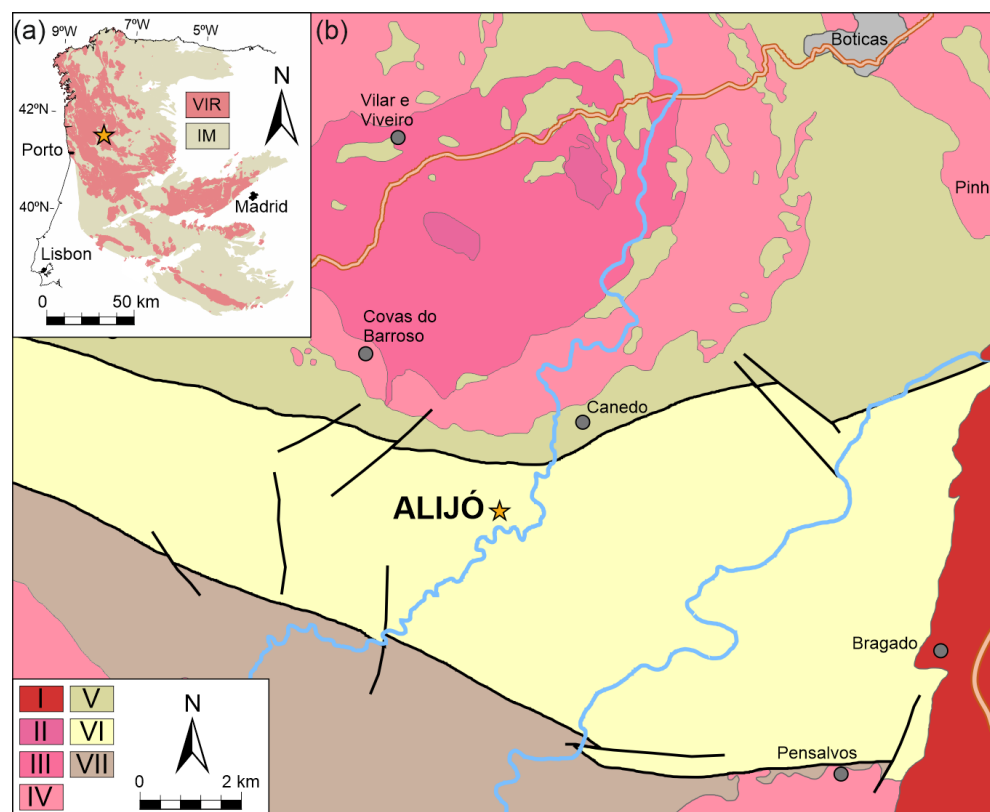


**Figure 1.** (a) Geological map of the Iberian Massif (IM; excluding the Ossa-Morena and South Portuguese zones), highlighting the Variscan Igneous Rocks (VIR). (b) Regional geological map of the Barroso-Alvão region: I: post-D3 biotite granites; II: syn-D3 biotite granites; III: syn-D3 biotite > muscovite granites; IV: syn-D3 two-mica granites; V: mica-schist and metagreywackes (lower parautochthon); VI: mica-schist/phyllites and quartzites (upper parautochthon); VII: dark schist and quartzites (upper parautochthon): Star: location of studied dyke. Based on [27,31–33].

Different types of late Variscan granitoids surround the BA Pegmatite Field, ranging from syn-D3 two mica granites to late/post-D3 biotite granites [34–38]. The syn-D3 plutons are represented in the area by the Barroso and Vila da Ponte granites, the Cabeceiras de Basto Pluton, and the Boticas/Leiranco granite, whereas late- to post-D3 massifs correspond to the Vila Pouca de Aguiar and Peneda-Gerês plutons [27,35,38–40]. The syn-D3 two-mica granites are peraluminous, and their origin has been proposed to be mainly from a crustal derivation, involving the melting of distinct metasedimentary and/or metaigneous sources [35,41]. By contrast, the genesis of the biotite dominant late- to post-D3 granitoids has been attributed to mantle-derived magmas in diverse ways, from hybridization of mantle-derived juvenile magmas with crustal melts/rocks to the melting of metabasic lower crustal protoliths [35,42,43] (Figure 1).

#### *Pegmatites from Barroso–Alvão*

The pegmatites from the BA Pegmatite Field are unevenly distributed in the region. They form local swarms of various sizes, up to 300 m in outcrop length. Their width is variable, from less than a few meters to up to 30 m across. These pegmatites display varied structures in terms of emplacement, some are flat-lying, whereas others occur gently or steeply dipping. Typically, these pegmatites cut discordantly through the host rock, showing sharp contacts. According to [44,45], five different groups of granitic pegmatites are identified in BA:

- (1) Intragranitic pegmatites with quartz, feldspar, muscovite, biotite, minor tourmaline, beryl, garnet, fluorapatite, chlorite, and zircon.

- (2) Barren pegmatites with quartz, feldspar, muscovite, minor biotite, fluorapatite, beryl, tourmaline, chlorite, zircon, pyrite, and monazite-(Ce).
- (3) Spodumene pegmatites with quartz, feldspar, spodumene, muscovite, minor columbite group minerals (CGM), fluorapatite, montebrasite, triphylite, phosphoferrite, dufrénite, fairfieldite, chlorite, tourmaline, zircon, uraninite and sphalerite. The selected aplite-pegmatite body from Alijó belongs to this third group.
- (4) Petalite pegmatites with quartz, feldspar, petalite, muscovite, minor cassiterite, CGM, fluorapatite, montebrasite, ferrisicklerite, eosphorite, pyrite, sphalerite, uraninite, monazite-(Ce), autunite and xenotime.
- (5) Lepidolite pegmatites with albite, lepidolite, and muscovite, minor cassiterite, CGM, fluorapatite, zircon, and goyazite.

### 3. Materials and Methods

Representative samples from 8 different parts of the selected dyke were collected for the present study in a 32 m-thick section perpendicular to the strike of the dyke. A total of 23 host rock samples were collected following the procedures of the H2020 GREENPEG project, taking samples systematically in a section perpendicular to the strike of the dykes, up to 35 m far from the dyke (location in Supplementary Materials; more details for the sampling procedure are provided in [18]). Among those host rock samples, four were collected several hundred meters away from the pegmatite as ‘control-samples’, in order to represent non-metasomatized compositions for the metasedimentary rocks.

Thirty-five polished sections were made from representative samples of the mineralized pegmatite and its host rocks for petrographic study, which was carried out using a Leica DM LP model polarizing microscope, Leica Microsystems Pty Ltd, Lane Cove West, Australia fitted with a CCD camera at the Geology Department of the University of the Basque Country UPV/EHU.

#### 3.1. Electron Microprobe (EMP) Analysis

Over 300 EMP analyses were obtained from polished thin sections using a Camebax SX-100 EMP at the Raimond Castaing Centre of the University of Paul Sabatier (Toulouse, France). The operating conditions were a voltage of 15 kV and a beam current of 10 nA (20 nA for phosphate minerals). The calibration standards used were synthetic SiO<sub>2</sub> (Si), synthetic MnTiO<sub>3</sub> (Ti, Mn) wollastonite (Ca) corundum (Al), hematite (Fe), albite (Na), orthoclase (K), fluorite (F), graftonite (P), periclase (Mg), synthetic chromite (Cr), synthetic glass of Rb<sub>2</sub>O (Rb) and Cs<sub>2</sub>O (Cs), synthetic BaTiO<sub>3</sub> (Ba), sphalerite (Zn), and tugtupite (Cl). Data were reduced using the procedure outlined in [46], and analytical errors estimated at ±1%–2% for major elements and ±10% for minor elements. Complete results can be found in the Supplementary Materials (SM).

#### 3.2. Whole-Rock Geochemical Analysis

A total of 24 samples were sent to Activation Laboratories Ltd. (Ancaster, ON, Canada) for whole-rock major and trace element analyses. For the pegmatite, a representative sample was obtained by crushing 15 kg of different proportional parts of the pegmatite to a nominal grain size of 1 cm at the Geology Department of the UPV/EHU. In the case of the 23 host rock samples, they were cut to obtain representative sub-samples of 300 g. Each sample was then crushed up to 80% (passing 2 mm), split using a riffle splitter (250 g), and pulverized up to 95% (passing 105 µm) using a mild steel pulverizer.

Major and trace element concentrations were obtained via different analytical techniques. To obtain major element concentrations, as well as Zr, Sc, Hf, and Lu concentrations, a lithium metaborate/tetraborate fusion was performed to dissolve the entire sample. Major elements were measured using X-ray fluorescence (Actlabs, Ancaster, ON, Canada), whereas Sc and Zr were analyzed by inductively coupled plasma—optical emission spectrometry (ICP-OES, Actlabs, Ancaster, ON, Canada), and Hf and Lu by ICP—mass spectrometry (MS, Actlabs, Ancaster, ON, Canada). Concentrations of the remaining trace

elements were also measured by ICP-MS, but with a previous sodium peroxide fusion. Fluorine concentrations were analyzed using an ion-selective electrode (ISE, Actlabs, Ancaster, ON, Canada) following a lithium borate fusion and dissolution in dilute nitric acid.

## 4. Results

### 4.1. Field Characterization of the Spodumene-Bearing Dyke from Alij6

The studied aplite-pegmatite body from Alij6 is a subvertical discordant body with an approximate strike of N155° E and variable thickness (5 to 30 m). This heterogeneous dyke is composed mainly of quartz, plagioclase, K-feldspar, spodumene, and white mica, with accessory tourmaline, phosphate minerals, eucryptite, beryl, cookeite, and CGM. According to [47], this dyke may be classified as an LCT pegmatite of the complex type and the spodumene subtype. Aplitic and pegmatitic facies are distributed heterogeneously inside the dyke, typically with an abrupt transition between them. Quartz and plagioclase compose mainly the aplitic units, whereas K-feldspar occurs randomly distributed. On the contrary, plagioclase and K-feldspar ( $\pm$ quartz) are the main rock-forming minerals in the pegmatitic units. Locally, spodumene becomes the main mineral phase.

One of the most remarkable petrographic features of this dyke is the abundance of unidirectional solidification textures (UST). In the aplitic units, a subvertical layering is commonly observed parallel to the contact with the host rocks, with alternating ( $\sim$ 1 cm thick) quartz + plagioclase-rich and plagioclase-rich layers (crystal sizes in the range of 1–3 mm) (Figure 2a). In the pegmatitic facies, plagioclase crystals often exhibit a combed texture, with the axis of the crystals growing perpendicularly to the contact with the host rocks (Figure 2b). Less frequently, spodumene crystals also appear as combed crystals.

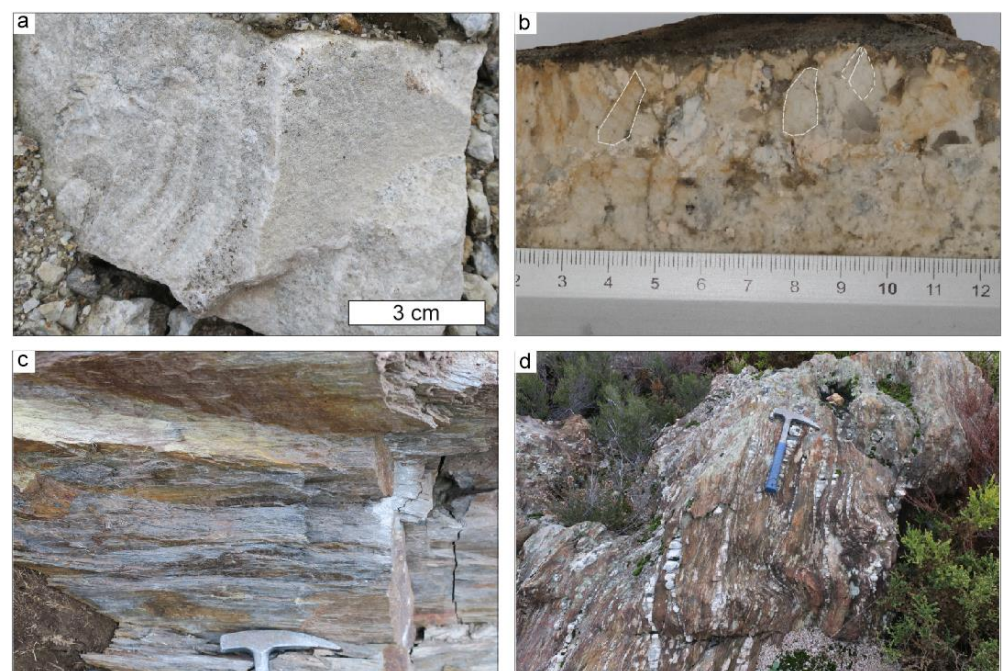


**Figure 2.** (a) Layered structure in an aplitic sample alternating quartz + plagioclase and plagioclase-rich layers. (b) Hand sample with a pegmatitic texture, exhibiting combed feldspars marked with dashed lines. (c) Representative outcrop of the pelitic host metasediments. (d) Field photograph of an outcrop showing psammitic layers in a mainly pelitic lithology.

The Alij6 spodumene-bearing aplitite-pegmatite body intrudes discordantly into a metasedimentary sequence that includes phyllites and mica-schists interlayered with black schists, lydites, and some quartz-phyllites and calc-silicate rocks of upper Ordovician to lower Devonian age [30] (Figure 2c,d). Broadly, these metasediments can be classified as pelitic (mica-rich and quartz/feldspar-poor) and psammitic (mica-poor).

These metasediments were later affected by the Variscan Orogeny, with the respective metamorphic overprint.

#### 4.2. Petrography and Mineral Chemistry of the Spodumene Pegmatite

The mineralogy of the studied pegmatitic body predominantly consists of quartz, plagioclase, K-feldspar, spodumene, and muscovite. Additionally, it contains accessory minerals such as tourmaline, phosphate minerals, eucryptite, beryl, cookeite, and members of the columbite group (Figure 3).

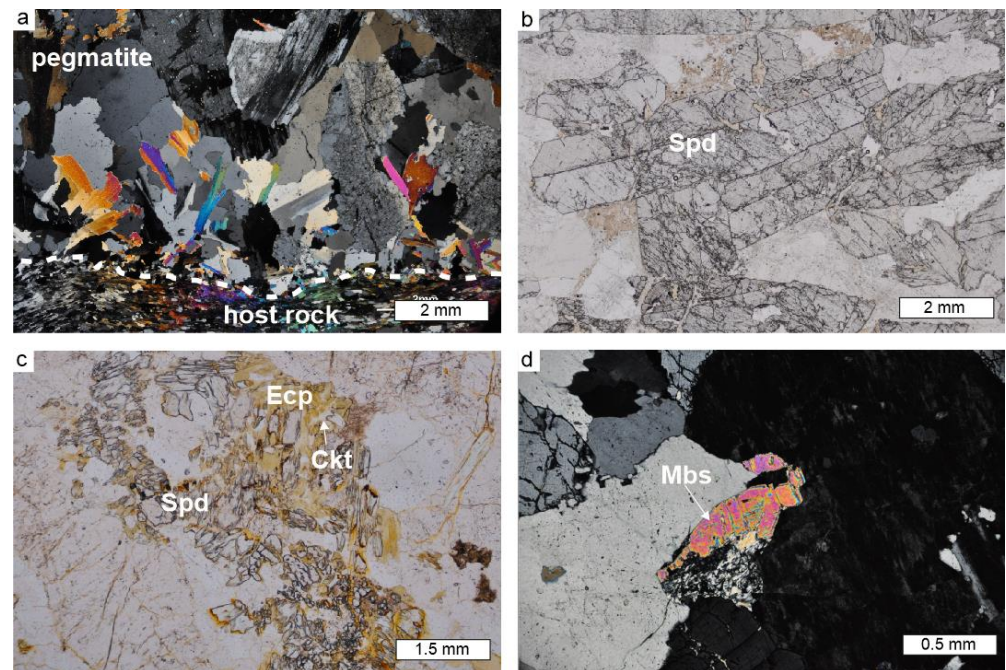


**Figure 3.** (a) Microphotograph of combed micas growing from the contact with the host rock marked by dashed line. (b) Euhedral spodumene crystals of up to 8 mm. (c) Eucryptite (Ecp) (yellowish) and cookeite (Ckt) (uncolored) replacing spodumene (Spd) crystals, with some relicts of Spd. (d) Anhedral crystal of montebrasite (Msb) with a slight twinning.

Feldspars constitute a volumetrically important part of the studied dyke, with albite ( $Ab_{98}\text{--}Ab_{99.8}$ ) being the most common term (Supplementary Materials). Albite occurs as fine to coarse subhedral crystals, with the biggest ones often growing perpendicularly to the dyke contacts. The chessboard texture or myrmekite intergrowths have been described. Potassium feldspar ( $Or_{92}\text{--}Or_{98}$ ) occurs as subhedral to anhedral crystals, varying in size from very fine to coarse (<5 cm). Some crystals display inclusions of quartz and/or micas, whereas others display Carlsbad or cross-hatched tartan pattern twinning. Phosphorous contents reach up to 0.43 wt.% and 0.36 wt.% ( $P_2O_5$ ) in K-feldspar and plagioclase, respectively. A negative correlation between Si and P + Al suggests the influence of the berlinite substitution type for the incorporation of P in the structure of these alkali feldspars (Figure 4a). Rubidium concentrations reach up to 2469 ppm in K-feldspar and below the detection limit in plagioclase.

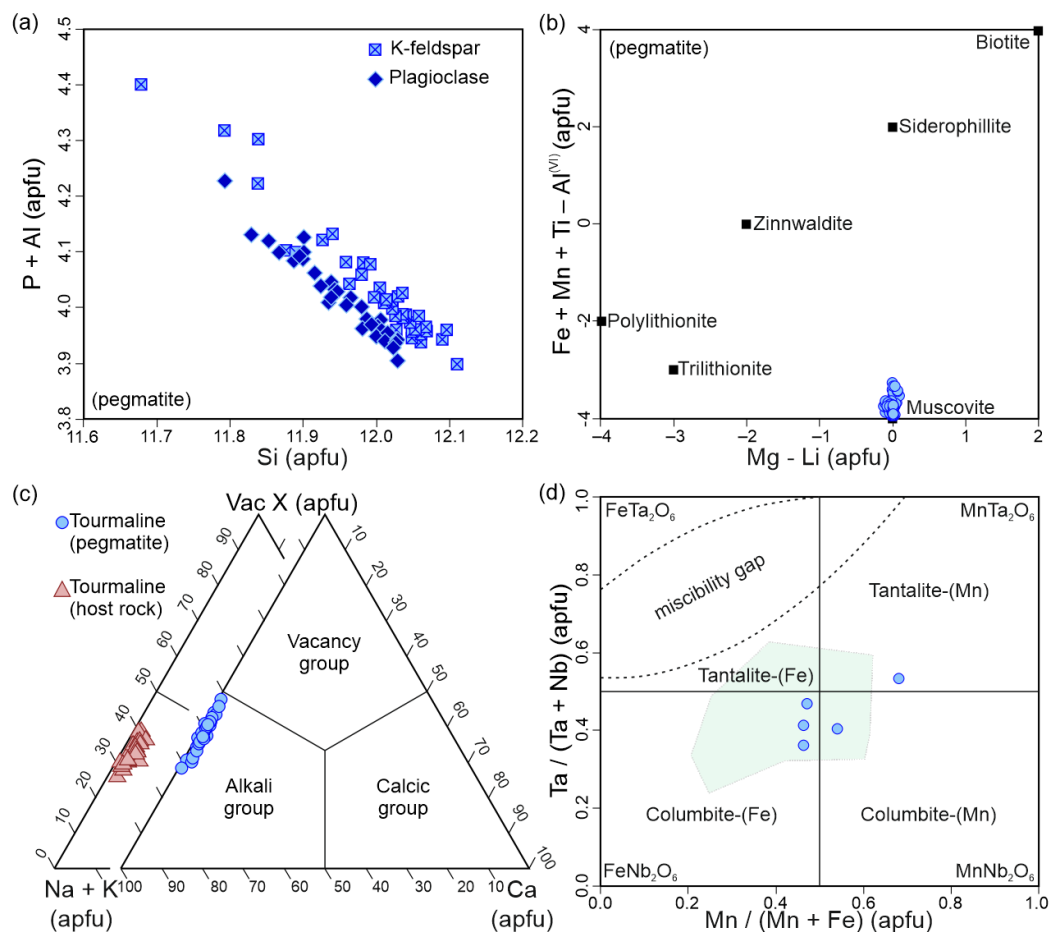


**Figure 4.** (a) Binary Si vs. P + Al diagram of K-feldspar and plagioclase from the Alijé pegmatite. (b) Binary Mg – Li vs. Fe + Mn + Ti + Al<sup>VI</sup> diagram of analyzed micas (based on [48]). (c) Ternary Na + K vs. Ca vs. vacancy (X site) classification diagram of analyzed tourmaline crystals. (d) Quadrilateral Mn/(Mn + Fe) vs. Ta/(Ta + Nb) plot of analyzed CGM from the Alijé pegmatite. Analyses of CGM from other localities from BA are also shown in green for comparison (data from [44]).

White mica crystals are fine-grained (<1 cm), subhedral, and usually tabular (less frequently radial). Close to the contacts with the host rocks, micas with combed textures grow perpendicularly to them (Figure 3a). Occasionally, primary crystals show “patchy zoning”. Analyzed micas fall in the muscovite field *sensu stricto* of the [48] classification diagram (Figure 4b; Supplementary Materials). Overall, Rb and Cs contents in micas reach up to 8961 ppm and 1792 ppm, respectively, whereas the Li content does not exceed 1000 ppm (Supplementary Materials).

Spodumene is the main Li-bearing rock-forming mineral phase in Alijé. The primary spodumene crystals are euhedral to subhedral with a medium to coarse grain size (<3 cm) (Figure 3b). As with other main mineral phases, these prismatic crystals may also grow perpendicularly to the contact with the host rock, showing a combed texture. Anhedral fine-grained secondary spodumene crystals are also common, containing small sub-rounded quartz crystals as a result of petalite replacement. Aggregates of spodumene crystals with an acicular habit, showing vermicular textures oriented around coarser crystals, have also been found. Eucryptite, as a low-PT Li-aluminosilicate, occurs as an accessory phase, as very fine-grained aggregates of anhedral crystals, together with albite and/or K-feldspar. These very fine-grained aggregates commonly replace pseudomorphically previous spodumene crystals, with small relicts of spodumene in the interior (Figure 3c). Sometimes, eucryptite

also occurs together with phyllosilicates such as cookeite, a frequent product of spodumene alteration (Figure 3c).

Tourmaline occurs as an accessory phase, mainly in the aplitic units of the dyke. It shows a fine to medium crystal size and appears as euhedral to subhedral crystals with a prismatic or acicular habit, apparently with no preferred orientation. According to the X-position occupancy [49,50], analyzed tourmalines are alkaline (Figure 4c). Chemical data showed 9.97–12.84 wt.% and <0.09 wt.% of FeO and MgO, respectively, allowing them to be classified as Fe-rich term schorl (Supplementary Materials). Instead of Mg, Li is present in tourmaline from the dyke ( $\text{Li}_2\text{O}$  0.28–0.8 wt.%), belonging to the schorl-elbaite series and evolving via the  $\text{LiAl}(\text{Fe})_2$  exchange vector.

Phosphate minerals appeared scattered, predominantly in the aplitic unit. In general, these accessory phases appear as subhedral to anhedral fine crystals and display brownish to yellowish color tones. Apatite is the most common phosphate, comprising chlorapatite (1.48–3.71 wt.% of Cl) with dark brown shades and a prismatic habit, and light brown to beige fluorapatite (2.3–3.46 wt.% of F) (Supplementary Materials). In general, MnO and FeO contents are high (1.41–6.75 wt.% and 1.25–4.44 wt.% respectively), with chlorapatites richer in Mn (~5 wt.%) and fluorapatites in Al (1.19–5.32 wt.%). Apatite crystals with low F and Cl could be classified as hydroxyapatites. Measured concentrations of Sr reach up to 1.12 wt.% (SrO). Regarding the amblygonite group minerals, they show a marked twinning (Figure 3d). Taking into account the low values of F (<1.4 wt%), these accessories correspond to almost pure montebrasite-term (Supplementary Materials).

Columbite group minerals from the studied dyke occur as an accessory phase. These fine-grained tabular crystals show homogeneous Mn/(Mn + Fe) and Ta/(Ta + Nb) ratios close to 0.5 (Supplementary Materials). Based on their composition, most of the analyzed crystals may be classified as columbite-(Fe) (Figure 4d).

#### 4.3. Petrography and Mineral Chemistry of the Host Rock

The studied host rock samples were composed of mica-schists, metagreywackes, quartzites, and phyllites that form a metamorphosed psammopelitic sequence (Figure 2c,d). In the pelitic samples, a well-developed slaty cleavage was observed (Figure 5a). In these samples, muscovite, biotite, and quartz were the main mineral phases whereas oxides, apatite, and garnet corresponded to the most common accessory phases (Figure 5a). Contrarily, the psammitic samples were mainly composed of quartz, with significantly smaller amounts of muscovite and biotite, with oxides as accessory minerals that appeared essentially in the pelitic layers (Figure 5b). Some samples corresponded to intermediate terms, with nearly equal proportions of micas and quartz (Figure 5c). Scattered biotite and garnet porphyroblasts were common in many samples, with relatively greater crystal sizes (Bt up to 2 mm, Grt up to 1.5 mm) (Figure 5d).

Close to the contact with the pegmatite, well-developed tourmalinization was observed in the pelitic samples and/or layers, with up to 1.5 cm long euhedral/subhedral tourmaline crystals that become gradually smaller in the samples collected further from the contact (Figure 5e). There were notable compositional differences between the tourmaline from the dyke and that found in its host rocks. Analyzed tourmaline crystals from the host rocks showed relatively lower FeO (8.94–10.97 wt.%) and higher MgO (2.75–3.9 wt.%) contents, belonging to the schorl-dravite series (Supplementary Materials).

Also close to the pegmatite contact, irregular masses of greisen formed mainly by quartz and muscovite were locally observed. The crystal size in these bodies (up to 3 mm) was greater than that of the metasedimentary host rocks (Figure 5f).

#### 4.4. Whole Rock Geochemistry

The studied aplite-pegmatite body showed relatively high  $\text{SiO}_2$  (75.62 wt.%),  $\text{Al}_2\text{O}_3$  (16.05 wt.%),  $\text{Na}_2\text{O}$  (3.18 wt.%), and  $\text{P}_2\text{O}_5$  (0.23 wt.%) contents, resulting in a strongly peraluminous and perphosphorous nature ( $A/\text{CNK} = 2.1$ ; normative apatite = 0.18; Table 1). As expected, MgO (0.03 wt.%),  $\text{Fe}_2\text{O}_3^{\text{t}}$  (0.34 wt.%),  $\text{TiO}_2$  (0.01 wt.%), and CaO (0.1 wt.%) con-



centrations are low, leading to a low maficity (B) parameter in the B-A diagram (Figure 6a). Moderate concentrations of  $K_2O$  (2.05 wt.%) lead to a  $K_2O/Na_2O$  ratio lower than unity (0.67). Regarding trace element composition, the studied dyke showed relatively low contents of F (100 ppm), but significantly high contents of Li (8480 ppm) (Figure 6b). The ratios  $K/Rb$  (27) and  $Nb/Ta$  (1.6) were in the range of Iberian-enriched aplite-pegmatite bodies (Figure 6c). In addition to Li, Nb, and Ta, concentrations of other trace elements such as Rb, Cs, Be, Sn, Ge, U, and Tl were significantly high as well, contrasting with commonly low contents of Ba, Sr, Zr, Y, Th, and REE (Figure 6e; Table 1).

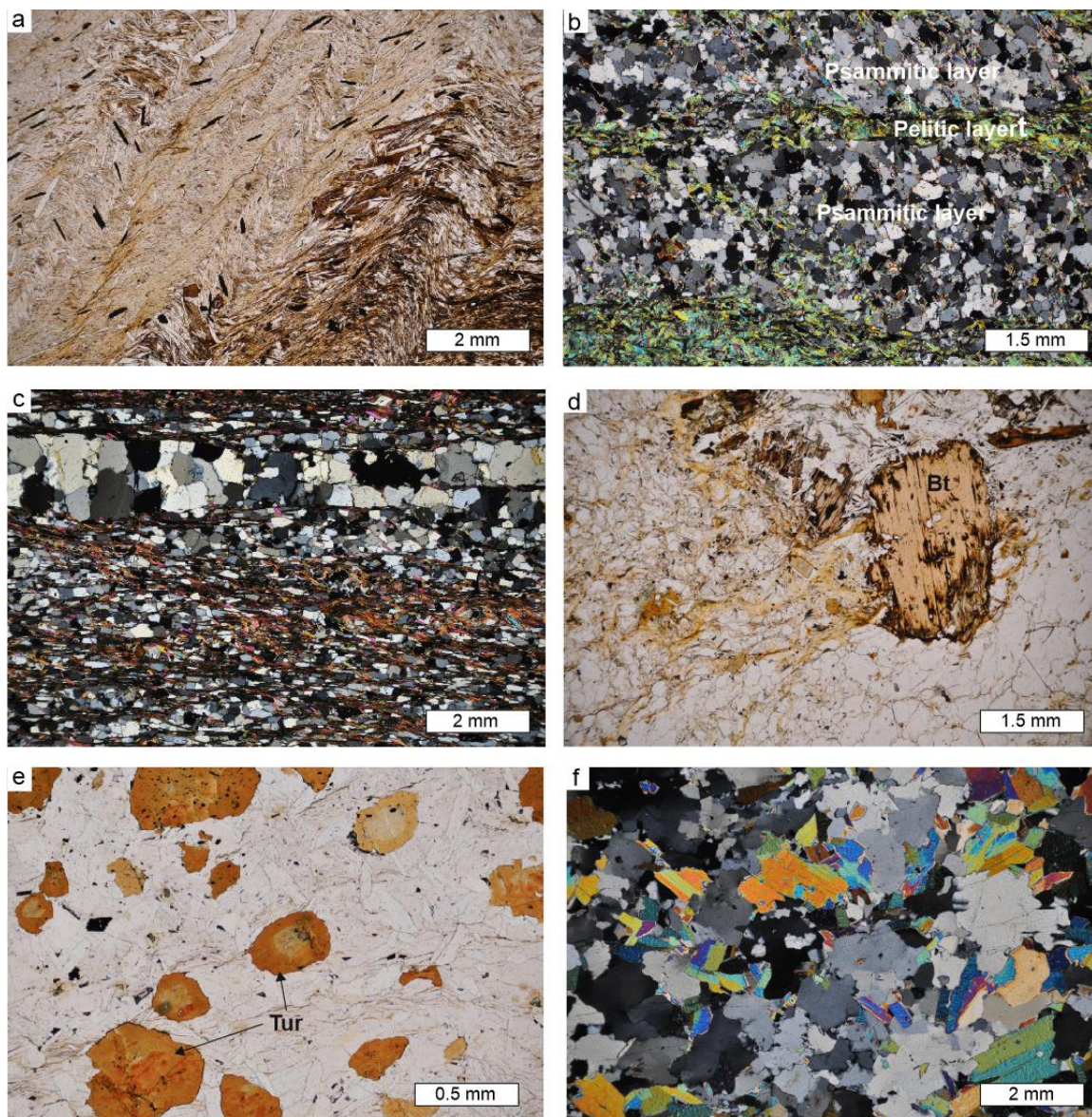


**Figure 5.** (a) Microphotograph of a pelitic (mica-rich) host rock sample, with a marked original slaty cleavage and a well-developed crenulation cleavage. (b) Alternating psammitic (quartz-rich) and pelitic layers in a psammitic host rock. (c) Microphotograph of an intermediate sample, with a greater mica proportion compared with the psammitic samples. (d) Porphyroblast of biotite (Bt) from the host rock. (e) Small tourmaline (Tur) crystals formed in the pelitic layers of the host rocks relatively close to the pegmatite. (f) Representative microphotograph of a greisen sample.

**Table 1.** Major- (wt.%) and trace-element (ppm) whole rock geochemical analyses of studied rocks from Alij6.

(a)												
Type	met.	met.	met.	met.	met.	met.	met.	met.	met.	met.	met.	met.
Class.	lith.	wacke	sub-lith.	shale	lith.	lith.	lith.	shale	shale	shale	greisen	Shale
Sample	B-09	B-10	B-11	B-12	B-13	B-14	B-15	B-16	B-17	B-18	B-19	B-20
Dist. (m)	0 W	0.5 W	1 W	2 W	3 W	6 W	12 W	20 W	35 W	50 W	0 E	0.5 E
SiO <sub>2</sub>	78.36	75.49	90.49	61.3	84.53	82.18	81.62	64.49	65.6	67.91	70.1	56.41
TiO <sub>2</sub>	0.54	0.56	0.19	0.9	0.45	0.47	0.46	1.18	0.82	0.56	0.13	0.96
Al <sub>2</sub> O <sub>3</sub>	12.37	13.99	4.61	20.1	9.43	11.21	9.89	23.05	18.51	16.21	18.01	24.83
Fe <sub>2</sub> O <sub>3</sub> <sup>t</sup>	3.08	2.95	2.69	8.02	1.56	1.71	3.31	3.65	5.92	7.57	2.06	6.54
MnO	0.024	0.026	0.026	0.085	0.026	0.015	0.037	0.055	0.044	0.052	0.04	0.026
MgO	0.62	0.54	0.26	1.69	0.18	0.18	0.42	0.37	0.77	0.49	0.2	0.58
CaO	<0.01	<0.01	0.02	<0.01	<0.01	<0.01	<0.01	<0.01	<0.01	<0.01	0.79	<0.01
Na <sub>2</sub> O	0.22	0.2	0.06	0.23	0.14	0.16	0.17	0.28	0.28	0.23	0.37	0.28
K <sub>2</sub> O	2.9	3.68	1.01	4.47	2.49	2.85	2.71	4.42	4.45	3.7	4.62	6.22
P <sub>2</sub> O <sub>5</sub>	0.04	0.04	0.02	0.04	0.04	0.03	0.05	0.09	0.1	0.1	0.93	0.11
LOI	1.82	2.26	0.71	3.79	1.49	1.79	1.69	2.69	4.09	3.65	2.73	4.7
Total	99.97	99.74	100.09	100.63	100.34	100.6	100.36	100.28	100.58	100.47	99.98	100.66
F	600	500	<100	200	<100	<100	<100	<100	<100	<100	600	300
As	22	66	12	30	15	12	8	104	46	19	14	32
B	1430	430	60	80	90	90	180	150	90	90	350	240
Ba	481	642	179	823	477	532	539	814	940	689	170	1170
Be	11	<3	<3	<3	<3	<3	<3	<3	<3	<3	147	6
Cr	90	110	110	150	80	100	90	130	130	120	70	150
Cs	26.8	22.8	4.3	16.8	8.8	8.2	11	9.1	17.1	7.9	66.5	30.2
Ga	15.9	19.8	6	31.4	15.9	13.3	15.9	29.9	25.4	24.5	30.3	32.6
Ge	2.8	3.1	1.3	3.7	2.3	2.1	2.7	2.9	2.7	2.6	6.4	3.3
Li	288	294	104	400	99	105	123	105	190	113	264	472
Mo	5	6	9	3	3	6	3	1	<1	3	2	2
Nb	12.5	11.8	5	24.6	10.8	9.8	10	20.5	17.7	13.7	58.3	19.3
Ni	40	40	40	50	20	30	20	30	50	40	140	20
Pb	27.9	19.6	17.2	25.2	18.3	21.4	19.9	32.2	26.5	26	19.4	34.8
Rb	215	216	52.1	229	104	104	102	147	178	146	834	334
Sn	38	22.8	3.5	7.6	3.7	2.7	3	8.3	5	4.3	185	24.4
Sr	58	53	23	69	52	54	56	82	62	60	197	85
Ta	1.3	0.9	0.3	1.8	0.8	1.1	0.9	2.1	1.5	1.2	51.4	1.8
Th	17.5	14.4	5.5	20.4	18.3	14.9	16.2	30.9	19.5	14.7	3.3	22
Tl	1.5	1.6	0.3	1.5	0.5	0.6	0.5	0.6	0.8	0.5	4.4	1.7
U	4	3.6	1.3	3.5	2.6	2.5	3.3	6.6	4.5	4.1	7.6	4.2
V	52	63	17	128	32	35	38	71	78	71	16	121
W	5.9	5.8	1.9	6.9	3.6	5.1	4.3	5.7	7.6	5.4	5.4	16.9
Y	32	24.7	9.3	35	29.4	24	28.9	41.5	30.4	25.7	6.3	38.2
Zn	60	30	30	80	<30	30	30	40	60	60	60	100
La	41.8	40.3	13.2	59.3	36.5	34.6	43.3	55.5	45	38.1	8	59.2
Ce	90.6	80.8	27.3	116	77.7	70.2	91	119	89.3	79.2	16.7	112
Pr	11.1	10.1	3.3	14.8	9.8	8.5	10.5	13.8	11.1	10.2	1.9	13.9
Nd	37	32.9	12.2	48.1	32.1	32	35.9	52.9	40.5	32.6	7.6	50.5
Sm	8.3	8	2.3	9.1	6	5.2	7	9.1	7.1	8.2	1.6	10
Eu	1.6	1.6	0.4	1.6	1.3	1.5	1.6	1.7	1.3	1.3	0.7	1.5
Gd	6.3	5.4	2.3	7.9	5.4	4.8	6	7.7	6	5.5	1.2	7.2
Tb	0.9	0.8	0.2	0.9	0.9	0.7	0.7	1.2	1	0.9	0.2	1.1
Dy	5.1	4.8	1.8	5.9	4.8	4.2	4.9	6.9	5.5	4.3	1	6.3
Ho	1	1.1	0.3	1.3	1.1	0.8	1.1	1.4	1.1	0.8	<0.2	1.4
Er	3.2	2	1.1	2.9	2.6	2.3	3.2	3.3	3.3	2.6	0.5	3.8
Tm	0.5	0.4	0.1	0.5	0.5	0.4	0.5	0.6	0.5	0.4	<0.1	0.5
Yb	4	3.6	1.4	4.2	3.8	2.7	4.3	5	4.3	2.9	1.1	3.9
(b)												
Type	met.	met.	met.	met.	met.	met.	met.	Ctrl.	Ctrl.	Ctrl.	Ctrl.	Peg.
Class.	wacke	shale	lith.	lith.	wacke	shale	shale	lith.	shale	lith.	shale	Spd. Peg.
Sample	B-21	B-22	B-23	B-24	B-25	B-26	B-27	ALI-01	ALI-03	ALI-04	ALI-05	ALI-02
Dist. (m)	1 E	2 E	3 E	6 E	12 E	20 E	35 E	> 200	> 200	> 100	> 100	> 100
SiO <sub>2</sub>	71.31	54.76	78.18	81.2	73.52	63.31	63.12	77.92	60.16	81.57	59.14	75.62
TiO <sub>2</sub>	0.76	1.34	0.43	0.45	0.69	0.87	0.84	0.6	0.86	0.52	0.88	0.01
Al <sub>2</sub> O <sub>3</sub>	16.96	26.2	12.89	11.47	17.02	22.32	19.57	12.73	21.1	10.53	22.19	16.05
Fe <sub>2</sub> O <sub>3</sub> <sup>t</sup>	3.5	6.67	2.19	1.63	3.14	5.89	7.41	2.9	6.82	2.36	6.74	0.34
MnO	0.024	0.056	0.016	0.015	0.026	0.051	0.048	0.054	0.065	0.039	0.074	0.029
MgO	0.3	0.85	0.36	0.24	0.44	0.87	0.62	0.44	0.91	0.41	1.48	0.03
CaO	<0.01	<0.01	<0.01	<0.01	0.01	0.02	<0.01	<0.01	0.13	0.11	0.06	0.1
Na <sub>2</sub> O	0.21	0.24	0.16	0.15	0.18	0.24	0.38	0.14	0.26	0.15	0.28	3.18
K <sub>2</sub> O	4.34	5.28	3.33	3.11	3.1	3.96	4.93	3.73	6.13	3.03	6.69	2.05
P <sub>2</sub> O <sub>5</sub>	0.09	0.15	0.04	0.02	0.04	0.1	0.1	0.04	0.27	0.12	0.1	0.23
LOI	2.93	4.32	2.12	1.8	2.24	2.93	3.69	1.83	3.36	1.52	3.07	0.84
Total	100.42	99.87	99.72	100.09	100.41	100.56	100.71	100.38	100.07	100.36	100.7	98.48

Table 1. Cont.

F	<100	<100	<100	<100	<100	<100	200	<100	300	<100	200	<100
As	16	102	15	19	22	78	17	18	175	24	40	<5
B	170	180	90	80	150	170	280	40	80	170	170	20
Ba	788	1020	614	560	568	755	1090	647	900	422	968	6
Be	<3	3	<3	<3	4	4	<3	<3	4	<3	5	141
Cr	150	160	80	90	100	160	130	80	160	100	140	70
Cs	17.1	17	8.8	5.8	13.5	32.6	19.6	7.8	25.2	7.2	22.5	65.5
Ga	22.7	33.4	16.6	17.5	21.7	28.8	27.9	15.4	34.9	15	30.8	17.5
Ge	3	3.8	2.4	2.3	3	3.3	2.7	1.6	3.2	2.1	2.5	6.8
Li	355	676	167	129	298	497	231	44	108	50	130	8480
Mo	4	<1	1	2	<1	3	<1	<1	<1	2	2	2
Nb	16.5	24.9	10.8	11.4	12.4	18.6	18.6	12.5	20.2	13.1	19.6	46.5
Ni	50	30	20	20	40	70	30	20	30	30	40	20
Pb	26.8	43.7	23.5	22	22.1	28.2	33	17.2	31.1	18.8	28.5	12
Rb	200	232	132	101	127	190	214	138	289	121	287	628
Sn	11.1	7	3.5	3.4	4.2	15.1	13.3	3.1	4.8	2.9	5	50.1
Sr	85	89	69	57	66	99	91	49	76	48	68	103
Ta	1.7	2.2	0.7	0.8	1.4	1.7	1.4	1.2	1.7	0.9	1.7	28.8
Th	20.5	27.7	9.4	12.9	22.5	19.8	21	24	22.5	21.3	19.7	0.5
Tl	1.2	1.1	0.7	0.4	0.8	1.1	1.1	0.9	1.3	0.6	1.6	3.7
U	4.1	6.3	2.3	2.6	4.2	4.4	4.6	5.1	4.9	4.5	4.1	12.7
V	63	113	38	35	46	82	94	37	104	36	101	<5
W	10.9	11	7	5.8	4.4	8.7	7.2	4.4	7.6	3	8.9	1.3
Y	30.8	42.7	26.2	22.7	26	39.2	33	19.7	52.1	30.8	30	0.2
Zn	40	90	30	<30	60	80	110	<30	70	40	60	40
La	48.6	78.2	28.7	31.1	39.1	52.1	52.6	30.7	93.5	21.5	31	<0.4
Ce	95.5	154	63	69.2	83	110	111	61.6	193	48.9	61.6	<0.8
Pr	12.1	18.9	7.2	8.2	10.6	14.2	13.7	8.8	24.8	6.1	7.9	<0.1
Nd	37.2	66	28.3	28.2	32.9	50.8	42	28.6	83.4	21.5	26.6	<0.4
Sm	7.6	13.3	4.1	5.7	6.5	9.2	6.7	4.8	15.9	5.1	5.8	<0.1
Eu	1.8	2.7	1.2	1.1	1.5	2	1.6	1	3.3	0.9	1.1	<0.1
Gd	6.2	10.6	4.7	5.2	5.5	7.5	7.6	3	15.2	5.6	4.5	0.2
Tb	1.1	1.5	0.7	0.7	0.8	1.2	1	0.6	2.2	0.9	0.8	<0.1
Dy	4.9	7.6	3.8	4.1	4.5	6.6	6.3	3.3	9.5	5.7	4.7	<0.3
Ho	1.2	1.5	0.9	0.9	1	1.2	1.3	0.8	1.9	1.3	0.9	<0.2
Er	3.7	4.6	2.8	2.6	3.2	3.5	3	2.3	5.6	3.5	3	<0.1
Tm	0.5	0.8	0.3	0.4	0.4	0.5	0.6	0.5	0.7	0.7	0.5	<0.1
Yb	4	5	2.6	2.8	3.8	4.1	3.8	3.7	5.2	4.1	3.3	0.1

met. = metasomatized host metasedimentary rock; Ctrl. = control sample (non-metasomatized composition); Peg. = pegmatite; lith. = litharenite; Spd. Peg. = spodumene-bearing pegmatite.

The studied set of metasedimentary samples could be classified geochemically as shales (eight pelitic samples), litharenites-arkoses (eight psammite samples), and two intermediate wackes (Figure 6e). The SiO<sub>2</sub> contents were lower in the pelitic samples (55–68 wt.%) compared with the psammitic samples (76–91 wt.%), which were inversely correlated with the Al<sub>2</sub>O<sub>3</sub> contents (16–26 wt.% and 5–14 wt.%, respectively) (Table 1). The pelitic samples had the highest FeO<sup>t</sup> (3.6–8.0 wt.%) and K<sub>2</sub>O (3.7–6.2) concentrations (1.6–3.3 wt.% and 1.0–3.9 wt.% in psammitic samples). The contents of TiO<sub>2</sub>, MgO, Na<sub>2</sub>O, and P<sub>2</sub>O<sub>5</sub> were also higher in the metapelites as expected, and all of them were extremely poor in CaO (most of them presented values below the detection limit). Trace element composition also differed depending on their pelitic or psammitic nature, with overall higher concentrations of Ba, Sr, Y, Th, and REE in the pelitic samples (Figure 6d,f).

In the case of other trace elements, significant variations were observed when metasomatized and non-metasomatized samples were compared. These differences were greater in the case of pelitic samples, as they held higher absolute concentrations compared with psammitic samples. Despite the similar low F contents of <600 ppm for the complete set of samples (<100 ppm for most of them), some tourmalinized samples displayed high B contents of 500–1430 ppm, and many of the metasomatized pelitic samples displayed Li concentrations greater than 300 ppm (up to 676 ppm) (Figure 7a). These Li concentrations decreased with the distance from the pegmatite contact, up to values that resembled those of the non-metasomatized samples (about 50 ppm in psammites and around 100–130 ppm in pelites). Maximum concentrations of other trace elements such as Rb (<350 ppm), Cs (<35 ppm), and Sn (<40 ppm) were also measured in host metasediments close to the pegmatite contact (Figure 7b–d).

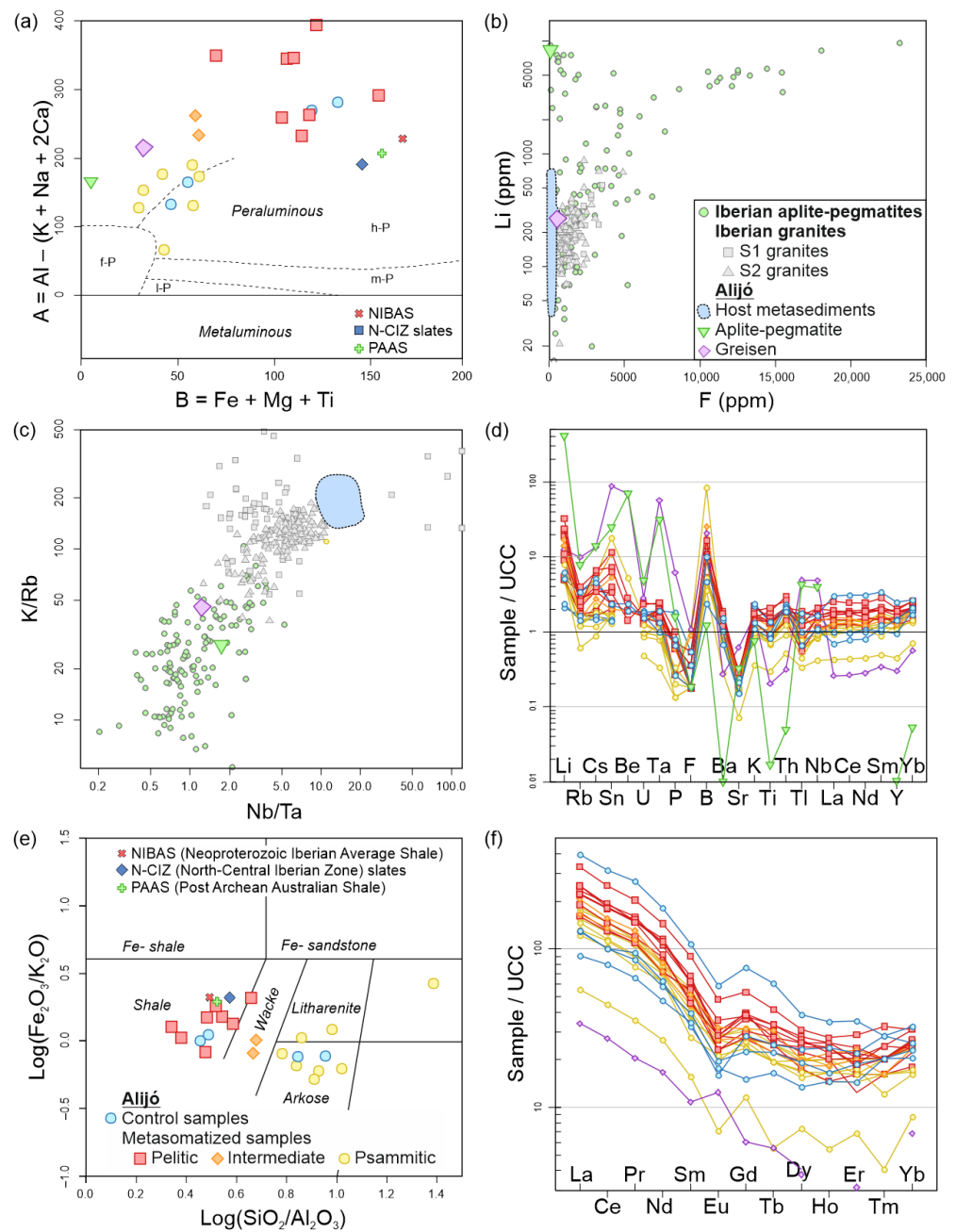


**Figure 6.** (a) Multicationic [B] vs. [A] diagram from [51] modified by [52], showing compositions of the selected aplite-pegmatite, greisen, and host rocks from Alijó. (b) Bivariate plot displaying F vs. Li (logarithmic) of the same set of samples (Iberian aplite-pegmatites, S1 granites, and S2 granites also shown for comparison; data taken from [13]). (c) Nb/Ta vs. K/Rb diagram (logarithmic) of the same three types of studied rocks. (d) Spider plots of the studied spodumene-pegmatite, host metasediments, and greisen normalized to the upper continental crust (UCC; [53]). (e) Classification diagram of siliciclastic sediments [54], showing compositions of the studied metasedimentary host rocks. Compositions of the Neoproterozoic Iberian Average Shale (NIBAS; [55]), average of North-Central Iberian Zone (N-CIZ) slates [56], and Post Archean Australian Shale (PAAS; [57]) are also displayed for comparison. (f) Chondrite-normalized [58] REE diagrams of the host metasediments.

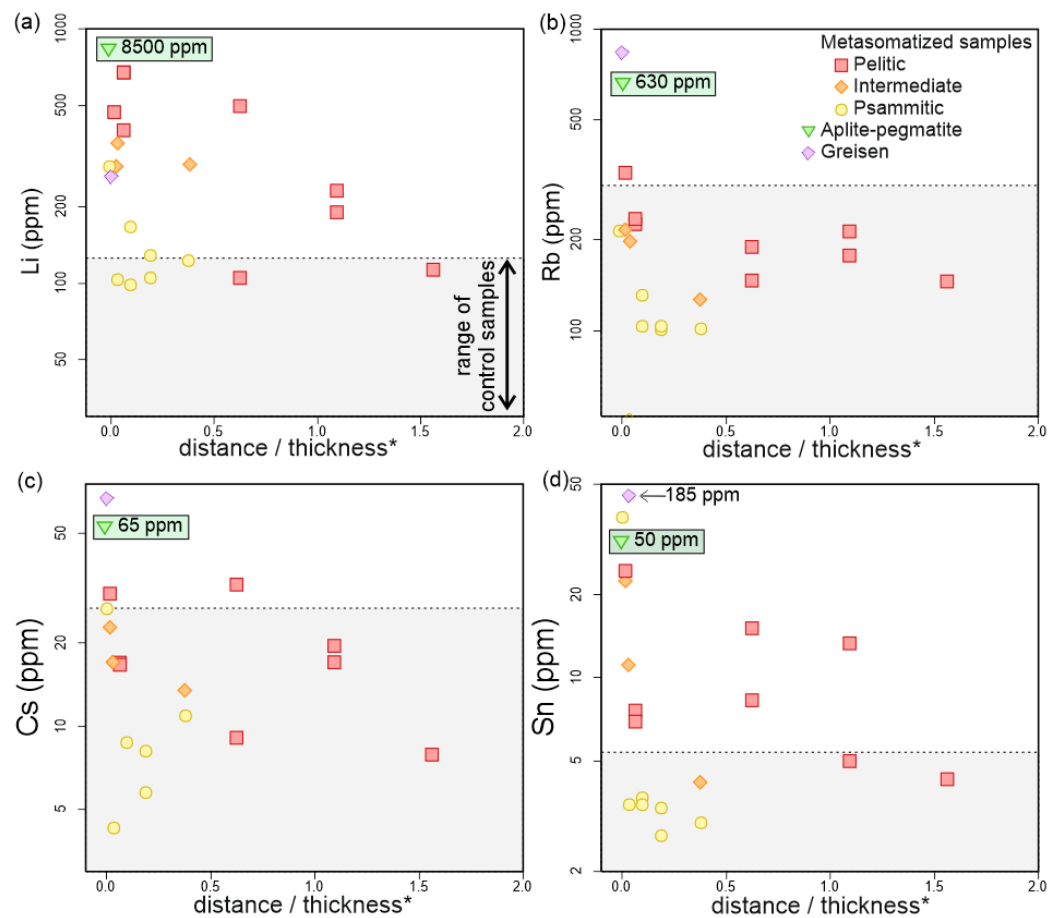


**Figure 7.** Binary diagrams showing (a) lithium, (b) rubidium, (c) cesium, and (d) tin concentrations in the studied host metasediments displayed relative to the distance from the dyke (\*), i.e., the distance from the dyke divided by the thickness of the dyke (range of non-metasomatized control samples also displayed in grey for comparison).

Regarding the greisen sample collected immediately after contact with the pegmatite, it showed remarkably high concentrations of  $P_2O_5$  (0.93 wt.%), F (600 ppm), B (350 ppm), Li (264 ppm), Be (147 ppm), Rb (834 ppm), Cs (66.5 ppm), Nb (58.3 ppm), Ta (51.4 ppm), Sn (185 ppm), and Tl (4.4 ppm) (Figure 7; Table 1).

## 5. Discussion

### 5.1. Internal Evolution of the Alijó Pegmatite

Several studies support that the structural state and texture of feldspars, as well as their chemical composition, may help to clarify the crystallization conditions of pegmatites [59–62]. The coexistence of albite and K-feldspar as individual phases suggests the subsolvus character of the studied body [63,64], as observed in the aplite-pegmatite body in Alijó. The crystallization of the two feldspars may be due to the increase in temperature of the solvus, associated with abundant Ca [65], or to the relatively high  $H_2O$  activity in the system, which would decrease the temperature of the solidus [63,66]. Considering the low Ca contents observed in the different mineral phases of the studied pegmatite, which are consistent with the extremely low Ca concentrations in the whole rock ( $CaO = 0.1$  wt.%), the second option seems to be the most plausible. The formation of greisen bodies and the tourmalinization observed close to the contact also attest to the relatively high  $H_2O$  contents in the pegmatitic system. On the other hand, the presence of cross-hatched twinning in microcline, as a result of the monoclinic–triclinic phase transition, indicates that the crystallization temperature of the dyke might have been above 450–500 °C [67,68].

Moreover, Li-aluminosilicates may help in interpreting the crystallization conditions [20,69]. The presence of both primary and secondary spodumene indicates that, in addition to crystallizing directly from the pegmatitic melt, some of the spodumene crystals in the dyke have been formed during subsolidus processes. These secondary crystals were most likely formed as the result of the replacement of primary petalite by a spodumene + quartz intergrowth [SQI texture] [70–73]. As shown by the P-T phase diagram for Li-aluminosilicates (Figure 8), the textural and paragenetic relationships suggest a rapid T decrease to allow the coexistence of primary and secondary spodumene with late eucryptite. Considering that the maximum conditions of regional metamorphism for the host rocks are ~3 kbar [30] and that the minimum crystallization temperature for K-feldspar to show lattice twins is 450–500 °C, the primary crystallization of the Alij6 pegmatite is proposed to have occurred within the range of 450–500 °C and 2–3 kbar (blue rectangle with dashed-line in Figure 8). This is consistent with the simultaneous crystallization of spodumene and ‘non-preserved’ petalite. The secondary mineral paragenesis of the studied dyke also indicates that the magmatic–hydrothermal transition in the evolution of the studied spodumene-bearing pegmatite continued up to eucryptite stability conditions (Figure 8). The replacement of spodumene crystals by eucryptite and cookeite is evidence of low-temperature metasomatism in a subsolidus stage. However, recent studies show that the stability of Li-aluminosilicates is more complex than previously thought, suggesting that P and T may not be the only factors controlling the crystallization of these minerals [72,73].

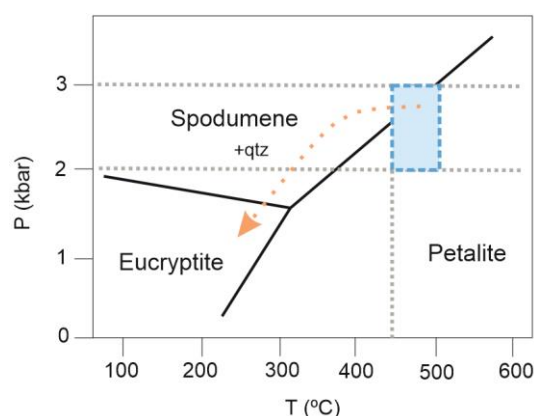


**Figure 8.** Temperature vs. pressure phase diagram for Li-aluminosilicates (modified from [69]).

Apart from textures, mineral chemistry provides valuable insights into the crystallization processes that occurred within the Alij6 dyke. The ratio K/Rb is considered a good indicator of the degree of fractionation in granitic-pegmatitic magmas, decreasing as the fractionation proceeds [74–76]. The K/Rb ratio in micas of spodumene pegmatites from BA is about 29 [45]. This value is relatively low, but it cannot be considered as extremely low as seen in highly fractionated pegmatites (K/Rb = 9 for lepidolite-bearing pegmatites, [45]). In other pegmatitic fields from the CIZ, the observed values are consistent. In Tres Arroyos, micas from the lepidolite-bearing pegmatites show K/Rb ratios of 20–4 [60]. Micas of the Li-mica-rich pegmatites from Fregeneda–Almendra show ratios of about 8–12, whereas spodumene pegmatites are in the range of 33–39 [77]. Considering these values, the ratio of 29 for micas from BA suggests a higher degree of fractionation compared with other spodumene-bearing pegmatites from the CIZ, but lower when compared with Li-mica and/or lepidolite-rich pegmatites from the same area. Whole-rock geochemistry is in line with this, with a K/Rb ratio of 27 calculated for the studied dyke, which is relatively lower than that obtained by [19] and that of spodumene-bearing pegmatites from Fregeneda–Almendra [K/Rb = 39–46], and higher than those of the Li-mica-rich pegmatites from Fregeneda–Almendra (K/Rb = 16–17) [78] and lepidolite-bearing dykes from Tres Arroyos (K/Rb = 7) [79].

Phosphate minerals also play a significant role as petrogenetic indicators in these granitic-pegmatitic environments [80–83]. Considering that Cl is a highly volatile element, and so, would easily separate from the melt once the system was opened [84], the crystallization of chlorapatite must have occurred before the opening of the system. The analyzed CGM crystals show slightly higher Ta/[Ta + Nb] and Mn/[Mn + Fe] ratios than the ones proposed for the spodumene subtype pegmatites from the Barroso-Alvão region [44]. However, all of them are in agreement with other CGM from spodumene-bearing pegmatites from the CIZ, such as the Fregeneda–Almendra pegmatite Field [77]. The small variation in the fractionation of Nb–Ta could be attributed to the presence of other Fe competitors such as schorl [85].

According to experimental data based on the correlation  $C_F^{\text{Montebrasite}} = 3.65C_F^{\text{melt}} + 0.07$  obtained by [86], the F concentration in the melt during crystallization would be below 0.27%. Such a low F contents in the melt, also evidenced by the absence of topaz and the presence only of montebrasite, would determine the principal Li-bearing minerals, crystallizing Li-aluminosilicate instead of lepidolite in the Alijó dyke.

### 5.2. External Metasomatism Caused by the Alijó Pegmatite

The magmatic–hydrothermal transition in pegmatite evolution is a complex, multi-stage process where silicate melt–hydrosaline melt–aqueous fluid immiscibility may occur as the pegmatitic melt cools (e.g., [87–90]). This transition in magmatic systems of granitic composition usually occurs when crystallization is already in an advanced stage, but in the case of volatile-rich shallow magmatic systems, early exsolution of fluid phases is also likely [91]. The nature of the exsolved fluid strongly depends on the nature of the pegmatitic melt, conditioning the availability of the elements that can partition into the fluid phase [92,93]. In the case of evolved terms of LCT pegmatites, the studied cases have shown that the pegmatite-derived metasomatizing fluids may cause enrichment in elements such as Li, Rb, Cs, F, B, Sn, Be, Tl, and W in the host rocks [15,17,18,94,95]. Despite varying in abundance compared to host rocks of other types of LCT-type enriched pegmatites, the host rocks that accommodate similar spodumene-rich pegmatites in this case study show enrichment in these same elements, especially in B, F, Li, Rb, Cs, and Sn (e.g., [17,18]).

The scarce presence of tourmaline within the studied spodumene-bearing dyke, together with the tourmalinization developed in the host metasedimentary rocks, particularly in close proximity to the pegmatite, suggest a relatively early opening of the system. This tourmalinization indicates B metasomatism in the host metasedimentary rocks, which caused the enrichment of up to 1430 ppm in the whole rock. Fluorine contents are also markedly higher in the host rocks close to the pegmatite contact (up to 600 ppm) and the greisen (up to 600 ppm) when compared with that in the spodumene-bearing pegmatite (<100 ppm) (Table 1). Although concentrations are not strictly correlated, Li enrichment seems to have occurred together with that of B and F. Lithium enrichment decreases gradually as the distance from the pegmatite increases, resembling a geochemical halo that differs significantly between pelitic (mica-rich) and psammitic (mica-poor) metasomatized samples (Figures 7a and 9a). Tin concentration is also remarkable outside the dyke, with a maximum value of 185 ppm observed in the greisen sample. Similarly to Li, Sn contents decrease with the distance in the metasomatized host metasediments, from a maximum value of 38 ppm in samples collected close to the dyke (Figure 7d). Rubidium and Cs enrichment in the metasedimentary host rocks is surprisingly minimal and is only recognizable in some of the pelitic samples. On the contrary, in the greisen sample, Rb and Cs concentrations reach high values of 834 and 66 ppm, respectively (Table 1). Despite the relatively low Li contents in the greisen (264 ppm) compared with metasomatized pelitic samples (400–700 ppm), the whole-rock geochemistry of the greisen properly reflects the overall enrichment prompted by the pegmatite-derived metasomatizing fluids. The studied greisen sample shows notably high contents of B, F, Li, Rb, Cs, Sn, Be, Nb, Ta, and Tl, with a total sum of B, F, Li, Rb, Cs, Sn of up to 2300 ppm (Figure 9b). The sum of these key trace

elements shows differences between mica-rich and mica-poor samples as well, with greater values in mica-rich samples (Figure 9b).

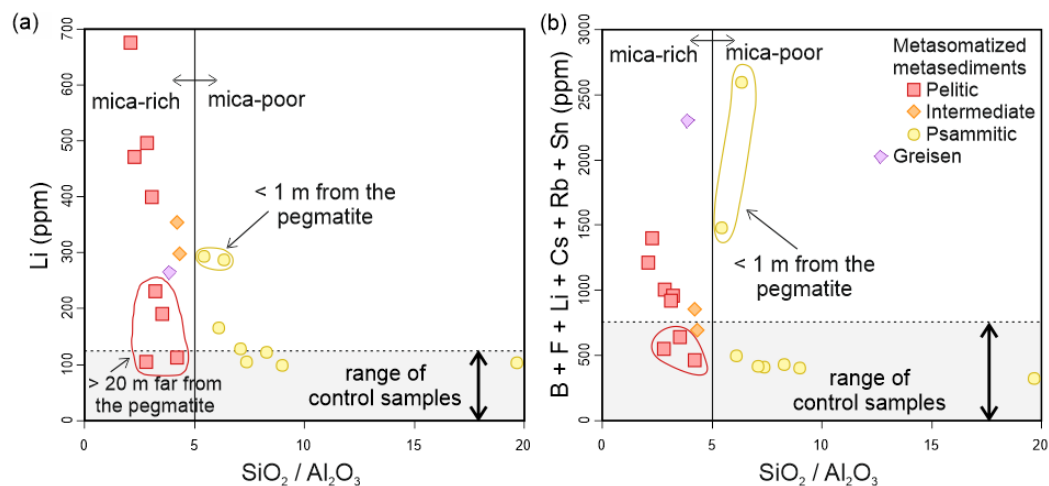


**Figure 9.** Binary  $\text{SiO}_2/\text{Al}_2\text{O}_3$  vs. Li (a) and  $\text{SiO}_2/\text{Al}_2\text{O}_3$  vs.  $\text{B} + \text{F} + \text{Li} + \text{Cs} + \text{Rb} + \text{Sn}$  (b) diagrams that show geochemical differences between mica-rich (pelitic) and mica-poor (psammitic) metasedimentary host rocks.

Despite the absence of clear concentration decreasing trends that may define geochemical halos around the studied spodumene-bearing pegmatite (the only exception could be Li), the metasomatic signature related to the pegmatite in the metasedimentary host rocks is consistent with other studied cases in central Iberia (e.g., [18]). The geochemistry of the pelitic samples collected close to the studied pegmatite, together with the geochemical composition of the greisen, indicate that at least B, F, Li, Rb, Cs, Sn, Be, Nb, Ta, and Tl were mobilized from the pegmatitic melt to the host rocks by the exsolved fluids. The early exsolution of a fluid phase from the pegmatitic melt and its subsequent escape into the nearby host rocks were probably facilitated by shallow emplacement conditions. The loss of flux elements such as  $\text{H}_2\text{O}$ , Li, F, and B may have induced a strong undercooling of the system, resulting in the formation of the UST observed in the Alijó pegmatite. This lowering of the solidus, together with a sudden decrease in pressure and temperature due to the shallow emplacement of the pegmatitic melt into open fractures, may have led to the formation of such textures, as suggested in experimental works [96–99]. In addition, the high concentrations of B and F in the exsolved fluids probably favored the formation of metal–ligand complexes, facilitating their transport from the pegmatite to the surrounding host rocks during fluid exsolution [100–103].

Based on the obtained geochemical data, certain inferences can be made regarding lithium exploration for the BA region. Considering the significant differences observed between pelitic and psammitic host metasedimentary rocks in terms of elemental enrichment, only the pelitic samples should be considered for litho-geochemical exploration studies. Apart from the visible tourmalinization in the field, which may only indicate close proximity to a dyke, the whole rock geochemical gains in pelitic host rocks may trace mineralized pegmatites at greater distances. Lithium contents greater than 300 ppm in this type of sample may indicate the presence of a Li-rich pegmatite but should be used in combination with other elements due to the lack of clear geochemical halos. We suggest the sum of B, F, Li, Rb, Cs, and Sn as a possible parameter to consider for Li exploration in BA, with an approximate minimum value of 1000 ppm (with all due caution) that may relate to a mineralized pegmatite in this region.



## 6. Conclusions

The spodumene-bearing pegmatite dyke from Alijó, located in the Portuguese Barroso–Alvão region, is an unzoned pegmatite enriched in elements such as Li, Cs, Rb, Be, Sn, Nb, Ta, Ge, U, and Tl, among others. Mineralogical data suggest a moderate to high degree of differentiation of the pegmatitic melt, which was emplaced under pressure conditions of approximately 2–3 kbar. Primary crystallization likely occurred at temperatures between 450–500 °C, with significant undercooling caused by (1) a sudden decrease in P-T conditions due to the shallow emplacement of the pegmatitic melt into open fractures, (2) the early exsolution of a fluid phase carrying flux elements such as F, B, and Li, or (3) the combination of both of them.

The escape of the exsolved fluid phase generated greisen bodies and induced external metasomatism in the surrounding metasedimentary host rocks. This study shows that the degree of metasomatism varies not only with the composition of the intruded pegmatite, as observed in other pegmatitic fields from CIZ [18], but also with the nature of the host rocks, which are generally classified as either pelitic (mica-rich) or psammitic (mica-poor). Whole-rock geochemistry reveals that pelitic samples exhibit a significantly higher enrichment of fluid-mobilized elements (B, F, Li, Sn, Be,  $\pm$ Rb, and  $\pm$ Cs) compared to psammitic elements collected at the same distances from the dyke. This suggests that, for lithochemical studies aimed at Li exploration, pelitic samples should be prioritized over psammitic ones. With all caution, we propose that whole rock Li concentrations greater than 300 ppm, together with a minimum value of 1000 ppm for the sum of B, F, Li, Rb, Cs, and Sn in pelitic metasediments from Barroso–Alvão, may indicate the presence of a mineralized pegmatite dyke in the area.

**Supplementary Materials:** The following supporting information can be downloaded at <https://www.mdpi.com/article/10.3390/min14070701/s1>.

**Author Contributions:** Conceptualization, I.G.-O., J.E.-M. and E.R.-R.; methodology, J.E.-M.; formal analysis, N.S.-L. and J.E.-M.; writing—original draft preparation, I.G.-O., N.S.-L. and J.E.-M.; writing—review and editing, I.G.-O., E.R.-R., A.L. and T.M.; visualization, I.G.-O. and J.E.-M.; supervision, E.R.-R.; project administration, E.R.-R.; funding acquisition, E.R.-R. All authors have read and agreed to the published version of the manuscript.

**Funding:** Financial support was provided by the European Commission’s Horizon 2020 Innovation Programme [grant agreement No 869274, project GREENPEG: New Exploration Tools for European Pegmatite Green-Tech Resources]; and University of the Basque Country UPV/EHU [grant GIU21/008]. N.S.L. is beneficiary of the Predoctoral Programme for the Formation of Non-Doctoral Research Staff of the Basque Government’s Department of Education.

**Data Availability Statement:** Data are contained within the article and Supplementary Materials.

**Acknowledgments:** The authors are grateful to three anonymous reviewers for their suggestions. The authors would like to acknowledge also Eric Xu for the editorial handling. The authors thank Grupo Lagoa for access to the Alijó pegmatite during this study.

**Conflicts of Interest:** The authors declare no conflicts of interest.

## References

1. Jaskula, B.W. *Minerals Yearbook: Lithium*; U.S. Geological Survey: Reston, VA, USA, 2017.
2. Gourcerol, B.; Gloaguen, E.; Melleton, J.; Tuduri, J.; Galieguea, X. Re-assessing the European lithium resource potential—A review of hard-rock resources and metallogeny. *Ore Geol. Rev.* **2019**, *109*, 494–519. [[CrossRef](#)]
3. Bibienne, T.; Magnan, J.-F.; Rupp, A.; Laroche, N. From Mine to Mind and Mobiles: Society’s Increasing Dependence on Lithium. *Elements* **2020**, *16*, 265–270. [[CrossRef](#)]
4. Moss, R.L.; Tzimas, E.; Kara, H.; Willis, P.; Kooroshy, J. *Critical Metals in Strategic Energy Technologies*; Institute for Energy and Transport European Commission: Luxembourg, 2011.
5. Linnen, R.L.; Van Litchervelde, M.; Černý, P. Granitic pegmatites as sources of strategic metals. *Elements* **2012**, *8*, 275–280. [[CrossRef](#)]
6. Simons, B.; Andersen, J.C.Ø.; Shail, R.K.; Jenner, F.E. Fractionation of Li, Be, Ga, Nb, Ta, In, Sn, Sb, W and Bi in the peraluminous Early Permian Variscan granites of the Cornubian Batholith: Precursor processes to magmatic-hydrothermal mineralization. *Lithos* **2017**, *278–281*, 491–512. [[CrossRef](#)]

7. European Commission. *Critical Raw Materials Resilience: Charting a Path towards Greater Security and Sustainability*; European Commission: Brussels, Belgium, 2020.
8. Müller, A.; Reimer, W.; Wall, F.; Williamson, B.; Menuge, J.; Brönnner, M.; Haase, C.; Brauch, K.; Pohl, C.; Lima, A.; et al. GREENPEG—Exploration for pegmatite minerals to feed the energy transition: First steps towards the Green Stone Age. *Geol. Soc. Lond. Spec. Publ.* **2022**, *526*, 27. [[CrossRef](#)]
9. Roda-Robles, E.; Pesquera, A.; Gil-Crespo, P.P.; Vieira, R.; Lima, A.; Garate-Olave, I.; Martins, T.; Torres-Ruiz, J. Geology and mineralogy of Li mineralization in the Central Iberian Zone (Spain and Portugal). *Mineral. Mag.* **2016**, *80*, 103–126. [[CrossRef](#)]
10. Simmons, W.B.; Webber, K.L. Pegmatite genesis: State of the art. *Eur. J. Mineral.* **2008**, *20*, 421–438. [[CrossRef](#)]
11. London, D. Ore-forming processes within granitic pegmatites. *Ore Geol. Rev.* **2018**, *101*, 349–383. [[CrossRef](#)]
12. Blundy, J.; Wood, B. Partitioning of trace elements between crystals and melts. *Earth Planet. Sci. Lett.* **2003**, *210*, 383–397. [[CrossRef](#)]
13. Roda-Robles, E.; Villaseca, C.; Pesquera, A.; Gil-Crespo, P.P.; Vieira, R.; Lima, A.; Garate-Olave, I. Petrogenetic relationships between variscan granitoids and Li-(F-P)-rich aplite-pegmatites in the Central Iberian Zone: Geological and geochemical constraints and implications for other regions from the European variscides. *Ore Geol. Rev.* **2018**, *95*, 408–430. [[CrossRef](#)]
14. Breiter, K.; Ďurišová, J.; Korbelová, Z.; Lima, A.; Vašinová Galiová, M.; Hložková, M.; Doshaba, M. Rock textures and mineral zoning—A clue to understanding rare-metal granite evolution: Argemela stock, Central-Eastern Portugal. *Lithos* **2022**, *410–411*, 106562. [[CrossRef](#)]
15. Linnen, R.; McNeil, A.; Flemming, R. Some thoughts on metasomatism in pegmatites. *Can. Mineral.* **2019**, *57*, 765–766. [[CrossRef](#)]
16. Roza-Llera, A.; Fuertes-Fuente, M.; Cepedal, A.; Martín-Izard, A. Barren and Li-Sn-Ta Mineralized Pegmatites from NW Spain (Central Galicia): A Comparative Study of Their Mineralogy, Geochemistry, and Wallrock Metasomatism. *Minerals* **2019**, *9*, 739. [[CrossRef](#)]
17. Barros, R.; Kaeter, D.; Menuge, J.F.; Škoda, R. Controls on chemical evolution and rare element enrichment in crystallising albite-spodumene pegmatite and wallrocks: Constraints from mineral chemistry. *Lithos* **2020**, *352–353*, 105289. [[CrossRef](#)]
18. Errandonea-Martín, J.; Garate-Olave, I.; Roda-Robles, E.; Cardoso-Fernandes, J.; Lima, A.; Ribeiro, M.A.; Teodoro, A.C. Metasomatic effect of Li-bearing aplite pegmatites on psammitic and pelitic metasediments: Geochemical constraints on critical raw material exploration at the Fregeneda–Almendra Pegmatite Field (Spain and Portugal). *Ore Geol. Rev.* **2022**, *150*, 105155. [[CrossRef](#)]
19. Lima, A. Estrutura, Mineralogia e Génese dos Filões Aplitopegmatíticos com Espodumena da Região do Barroso-Alvão (Norte de Portugal). Ph.D. Thesis, University Porto, Porto, Portugal; INPL, Nancy, France, 2000.
20. Charoy, B.; Noronha, F.; Lima, A.M.C. Spodumene—Petalite—Eucryptite: Mutual relationships and alteration style in Li-rich aplite–Pegmatite dykes from northern Portugal. *Can. Mineral.* **2001**, *39*, 729–746. [[CrossRef](#)]
21. Martins, T. Multidisciplinary Study of Pegmatites and Associated Li and Sn–Nb–Ta Mineralisation from the Barroso-Alvão Region. Ph.D. Thesis, University Porto, Porto, Portugal, 2009.
22. Farias, P.; Gallastegui, G.; González Lodeiro, F.; Marquínez, J.; Martín-Parra, L.M.; Martínez Catalán, J.R.; Pablo Maciá, J.G.; Rodríguez-Fernández, L.R. Aportaciones al conocimiento de la litoestratigrafía y estructura de Galicia Central. In *Memorias del Museo y Laboratorio Mineralógico y Geológico, de la Facultad de Ciencias*; Universidad de Oporto: Porto, Portugal, 1987; Volume 1, pp. 411–431.
23. Julivert, M.; Marcos, A.; Truyols, J. L'évolution paléogéographique du NW de l'Espagne pendant l'Ordovicien–Silurien. *Bull. Soc. Géol. Mineral. Bretagne* **1972**, *4*, 1–7.
24. Ribeiro, A.; Pereira, E.; Dias, R.; Gil Ibarguchi, J.I.; Arenas, R. Allochthonous Sequences. In *Pre-Mesozoic Geology of Iberia. IGCP-Project 233*; Dallmeyer, R.D., Garcia, E.M., Eds.; Springer: Berlin/Heidelberg, Germany, 1990. [[CrossRef](#)]
25. Valverde-Vaquero, P.; Marcos, A.; Farias, P. U–Pb dating of Ordovician felsic volcanics in the Schistose domain of the Galicia-Trás-os-Montes Zone near Cabo Ortegal (NW Spain). *Geol. Acta* **2005**, *3*, 27–37. [[CrossRef](#)]
26. Martínez Catalán, J.R.; Rubio Pascual, F.J.; Díez Montes, A.; Díez Fernández, R.; Gómez Barreiro, J.; Dias da Silva, I.; González Clavijo, E.; Ayarza, P.; Alcock, J.E. The late Variscan HT/LP metamorphic event in NW and Central Iberia: Relationships to crustal thickening, extension, orocline development and crustal evolution. In *The Variscan Orogeny: Extent, Timescale and the Formation of the European Crust*; Schulmann, K., Martínez Catalán, J.R., Lardeaux, J.M., Janousek, V., Oggiano, G., Eds.; Geological Society: London, UK, 2014; pp. 225–247. [[CrossRef](#)]
27. Ribeiro, M.A.; Martins, H.C.; Almeida, A.; Noronha, F. *Notícia Explicativa da Carta Geológica de Portugal na Escala 1:50,000—Folha 06C—Cabeceiras de Basto*; Serviços Geológicos de Portugal: Amadora, Portugal, 2000.
28. Noronha, F.; Ramos, J.M.F.; Rebelo, J.; Ribeiro, A.; Ribeiro, M.L. Essai de corrélation des phases de déformation hercyniennes dans le NW de la péninsule Ibérique. *Leidse Geol. Meded.* **1981**, *52*, 87–91.
29. Dias, R.; Ribeiro, A. The Ibero-Armorican Arc: A collisional effect against an irregular continent? *Tectonophysics* **1995**, *246*, 113–128. [[CrossRef](#)]
30. Ribeiro, M.A.; Ramos, R.; Noronha, F. Pegmatite-aplite veins of Barroso-Alvão Field. Lithostratigraphy and metamorphism of host rocks. In *Granitic Pegmatites: The State of the Art, Field Trip Guidebook*; Lima, A., Roda-Robles, E., Eds.; Universidade do Porto: Porto, Portugal, 2007.
31. Noronha, F.; Ribeiro, M.L. *Notícia Explicativa da Carta Geológica de Portugal na Escala 1:50,000—Folha 06A—Montalegre*; Serviços Geológicos de Portugal: Amadora, Portugal, 1983.
32. Teixeira, C. *Notícia Explicativa da Carta Geológica de Portugal na Escala 1:50,000—Folha 06B—Chaves*; Serviços Geológicos de Portugal: Amadora, Portugal, 1974.
33. Sant'Ovaia, H.; Ribeiro, M.A.; Martins, H.C.B.; Noronha, F. *Notícia Explicativa da Carta Geológica de Portugal na Escala 1:50,000—Folha 06D—Vila Pouca de Aguiar*; Serviços Geológicos de Portugal: Amadora, Portugal, 2011.

34. Ferreira, N.; Iglesias, M.; Noronha, F.; Pereira, E.; Ribeiro, A.; Ribeiro, M.L. Granitoides da Zona Centro Ibérica e o seu enquadramento geodinâmico. In *Geología de los Granitoides y Rocas Asociadas del Macizo Hesperico. Homenaje a L.C. García de Figuerola*; Bea, F., Carnicero, A., Gonzalo, J.C., López-Plaza, M., Rodríguez Alonso, M.D., Eds.; Libro Editorial Rueda: Madrid, Spain, 1987; pp. 37–51.
35. Dias, G.; Leterrier, J.; Mendes, A.; Simões, P.P.; Bertrand, J.M. U–Pb zircon and monazite geochronology of post-collisional Hercynian granitoids from the Central Iberian Zone (Northern Portugal). *Lithos* **1998**, *45*, 349–369. [[CrossRef](#)]
36. Sant’Ovaia, H.; Bouchez, J.L.; Noronha, F.; Leblanc, D.; Vignerresse, J.L. Composite-laccolith emplacement of the post-tectonic Vila Pouca de Aguiar granite pluton (northern Portugal): A combined AMS and gravity study. In *The Fourth Hutton Symposium on the Origin of Granites and Related Rocks*; Barbarin, B., Stephens, W.E., Bonin, B., Bouchez, J.-L., Clarke, D.B., Cuney, M., Martin, H., Eds.; Geological Society of America: Boulder, CO, USA, 2000; Volume 350. [[CrossRef](#)]
37. Almeida, A.; Martins, H.C.; Noronha, F. Hercynian acid magmatism and related mineralizations in northern Portugal. *Gondwana Res.* **2002**, *5*, 423–434. [[CrossRef](#)]
38. Cruz, C.; Sant’Ovaia, H.; Barolomeu Raposo, M.I.; Lourenço, J.M.; Almeida, F.; Noronha, F. Unraveling the emplacement history of a Portuguese post-tectonic Variscan pluton using magnetic fabrics and gravimetry. *J. Struct. Geotech.* **2021**, *153*, 104470. [[CrossRef](#)]
39. Almeida, A.; Leterrier, J.; Noronha, F.; Bertrand, J.M. U–Pb zircon and monazite geochronology of the Hercynian two mica granite composite pluton of Cabeceiras de Basto (Northern Portugal). *C. R. Acad. Sci.* **1998**, *326*, 779–785. [[CrossRef](#)]
40. Mendes, A.; Dias, G. Mantle-like Sr–Nd isotope composition of Fe–K subalkaline granites: The Peneda–Gerês Variscan massif (NW Iberian Peninsula). *Terra Nova* **2004**, *16*, 109–115. [[CrossRef](#)]
41. Teixeira, R.J.S.; Neiva, A.M.R.; Gomes, M.E.P.; Corfu, F.; Cuesta, A.; Croudace, I.W. The role of fractional crystallization in the genesis of early syn-D3, tin-mineralized Variscan two-mica granites from the Carrazeda de Ansiães area, northern Portugal. *Lithos* **2012**, *153*, 177–191. [[CrossRef](#)]
42. Dias, G.; Simões, P.P.; Ferreira, N.; Leterrier, J. Mantle and Crustal Sources in the Genesis of Late-Hercynian Granitoids (NW Portugal): Geochemical and Sr–Nd Isotopic Constraints. *Gondwana Res.* **2002**, *5*, 287–305. [[CrossRef](#)]
43. Villaseca, C.; Bellido, F.; Pérez-Soba, C.; Billström, K. Multiple crustal sources for post-tectonic I-type granites in the Hercynian Iberian Belt. *Miner. Petrol.* **2009**, *96*, 197–211. [[CrossRef](#)]
44. Martins, T.; Lima, A.; Simmons, B.; Falster, A.U.; Noronha, F. Geochemical fractionation of Nb–Ta oxides in Li-bearing pegmatites from the Barroso–Alvão Pegmatite Field, northern Portugal. *Can. Mineral.* **2011**, *49*, 777–791. [[CrossRef](#)]
45. Martins, T.; Roda-Robles, E.; Lima, A.; Parseval, P. Geochemistry and evolution of micas in the Barroso–Alvão pegmatite field, northern Portugal. *Can. Mineral.* **2012**, *50*, 1117–1129. [[CrossRef](#)]
46. Pouchou, J.L.; Pichoir, F. “PAP”  $\phi(\rho Z)$  procedure for improved quantitative microanalysis. In *Microbeam Analysis*; Armstrong, J.T., Ed.; San Francisco Press: San Francisco, CA, USA, 1985; pp. 104–106.
47. Cerný, P.; Ercit, T.S. The classification of granitic pegmatites revisited. *Can. Mineral.* **2005**, *43*, 2005–2026. [[CrossRef](#)]
48. Tischendorf, G.; Gottesmann, B.; Förster, H.-J.; Trumbull, R.B. On Li-bearing micas; estimating Li from electron microprobe analyses and an improved diagram for graphical representation. *Mineral. Mag.* **1997**, *61*, 809–834. [[CrossRef](#)]
49. Henry, D.J.; Novak, M.; Hawthorne, F.C.; Ertl, A.; Dutrow, B.L.; Uher, P.; Pezzotta, F. Nomenclature of the tourmaline-supergrroup minerals. *Am. Mineral.* **2011**, *9*, 895–913. [[CrossRef](#)]
50. Bosi, F. Tourmaline crystal chemistry. *Am. Mineral.* **2018**, *2018103*, 298–306. [[CrossRef](#)]
51. Debon, F.; Le Fort, P. A chemical–mineralogical classification of common plutonic rocks and associations. *Trans. R. Soc. Edinburgh Earth Sci.* **1983**, *73*, 135–149. [[CrossRef](#)]
52. Villaseca, C.; Barbero, L.; Herreros, V. A re-examination of the typology of peraluminous granite types in intracontinental orogenic belts. *Trans. R. Soc. Edinburgh Earth Sci.* **1998**, *89*, 113–119. [[CrossRef](#)]
53. Rudnick, R.L.; Gao, S. Composition of the continental crust. In *Treatise on Geochemistry*, 2nd ed.; Holland, H.D., Turekian, K.K., Eds.; Elsevier Science: Oxford, UK, 2014; Volume 4, pp. 1–51. [[CrossRef](#)]
54. Herron, M.M. Geochemical classification of terrigenous sands and shales from core or log data. *J. Sediment. Petrol.* **1988**, *58*, 820–829. [[CrossRef](#)]
55. Ugidos, J.M.; Sánchez-Santos, J.M.; Barba, P.; Valladares, M.I. Upper Neoproterozoic series in the Central Iberian, Cantabrian and West Asturian Leonese Zones (Spain): Geochemical data and statistical results as evidence for a shared homogenised source area. *Precambrian Res.* **2010**, *178*, 51–58. [[CrossRef](#)]
56. Villaseca, C.; Merino, E.; Oyarzun, R.; Orejana, D.; Pérez-Soba, C.; Chicharro, E. Contrasting chemical and isotopic signatures from Neoproterozoic metasedimentary rocks in the Central Iberian Zone (Spain) of pre-Variscan Europe: Implications for terrane analysis and early Ordovician magmatic belts. *Precambrian Res.* **2014**, *245*, 131–145. [[CrossRef](#)]
57. Taylor, S.R.; McLennan, S.M. *The Continental Crust: Its Composition and Evolution*; Blackwell Scientific Publications: Oxford, UK, 1985.
58. McDonough, W.F.; Sun, S.-S. The composition of the Earth. *Chem. Geol.* **1995**, *120*, 223–253. [[CrossRef](#)]
59. Neiva, A.M.R. Distribution of trace elements in feldspars granitic aplites and pegmatites from Alijó–Sanfins, northern Portugal. *Mineral. Mag.* **1995**, *59*, 35–45. [[CrossRef](#)]
60. Garate-Olave, I.; Roda-Robles, E.; Gil-Crespo, P.P.; Pesquera, A. Mica and feldspar as indicators of the evolution of a highly evolved granite-pegmatite system in the Tres Arroyos area (Central Iberian Zone, Spain). *J. Iberian Geol.* **2018**, *44*, 375–403. [[CrossRef](#)]
61. London, D.; Hunt, L.E.; Schwing, C.R.; Gutter, B.M. Feldspar thermometry in pegmatites: Truth and consequences. *Contrib. Mineral. Petr.* **2020**, *175*, 8. [[CrossRef](#)]

62. Liu, Y.; Qin, K.; Zhao, J.; Zhou, O.; Shi, R. Feldspar traces mineralization processes in the Qongjiagang giant lithium ore district, Himalaya, Tibet. *Ore Geol. Rev.* **2023**, *157*, 105451. [[CrossRef](#)]
63. Tuttle, O.F.; Bowen, N.L. Origin of Granite in the Light of Experimental Studies in the System  $\text{NaAlSi}_3\text{O}_8\text{--KAlSi}_3\text{O}_8\text{--SiO}_2\text{--H}_2\text{O}$ . *Geol. Soc. Am. Mem.* **1958**, *74*, 1–146. [[CrossRef](#)]
64. Parson, I. Feldspars defined and described: A pair of posters published by the Mineralogical Society. Sources and supporting information. *Mineral. Mag.* **2010**, *74*, 529–551. [[CrossRef](#)]
65. Carmichael, I.S.E.; Turner, F.J.; Verhoogen, J. *Igneous Petrology*; McGraw—Hill: New York, NY, USA, 1974; p. 739.
66. Tuttle, O.F. Origin of the contrasting mineralogy of extrusive and plutonic salic rocks. *J. Geol.* **1952**, *60*, 107–124. [[CrossRef](#)]
67. Smith, J.V. Chemical and textural properties. In *Feldspar Minerals*; Smith, J.V., Ed.; Springer: Berlin/Heidelberg, Germany, 1974.
68. Ribbe, P.H. *Feldspar Mineralogy*, 2nd ed.; De Gruyter: Berlin, Germany, 1983; p. 362.
69. London, D. Experimental phase equilibria in the system  $\text{LiAlSiO}_4\text{--SiO}_2\text{--H}_2\text{O}$ : A petrogenetic grid for lithium-rich pegmatites. *Am. Mineral.* **1984**, *69*, 995–1004.
70. Černý, P.; Ferguson, R.B. The Tanco pegmatite at Bernic Lake, Manitoba. IV. Petalite and spodumene relations. *Can. Mineral.* **1972**, *11*, 660–678.
71. Rossovskiy, L.N.; Matrosov, I.I. Pseudomorphs of quartz and spodumene after petalite and their importance to the pegmatite-forming process. *Dokl. Akad. Nauk SSSR* **1974**, *216*, 1135–1137.
72. Dias, F.; Ribeiro, R.; Gonçalves, F.; Lima, A.; Roda-Robles, E.; Martins, T. Calibrating a Handheld LIBS for Li Exploration in the Barroso–Alvão Aplite-Pegmatite Field, Northern Portugal: Textural Precautions and Procedures When Analyzing Spodumene and Petalite. *Minerals* **2023**, *13*, 470. [[CrossRef](#)]
73. Dias, F.; Lima, A.; Roda-Robles, E. Mutual relationships between spodumene and petalite from the Iberian Massif pegmatites: More than PT changes? *Can. Mineral.* **2019**, *57*, 731–732. [[CrossRef](#)]
74. Roda, E.; Pesquera, A.; Gil-Crespo, P.P.; Torres-Ruiz, J.; Fontan, F. Origin and internal evolution of the Li-F-Be-B-P-bearing Pinilla de Fermoselle pegmatite (Central Iberian Zone, Zamora, Spain). *Am. Mineral.* **2005**, *90*, 1887–1899. [[CrossRef](#)]
75. Marchal, K.L.; Simmons, W.B.; Falster, A.U.; Webber, K.L.; Roda-Robles, E. Geochemistry, mineralogy, and evolution of Li-Al micas and feldspars from the Mount Mica pegmatite, Maine, USA. *Can. Mineral.* **2014**, *52*, 221–233. [[CrossRef](#)]
76. Cao, C.; Shen, P.; Bai, Y.; Luo, Y.; Feng, H.; Li, C.; Pan, H. Chemical evolution of micas and Nb-Ta oxides from the Koktokay pegmatites, Altay, NW China: Insights into rare-metal mineralization and genetic relationships. *Ore Geol. Rev.* **2022**, *146*, 104933. [[CrossRef](#)]
77. Vieira, R.; Roda-Robles, E.; Pesquera, A.; Lima, A. Chemical variation and significance of micas from the Fregeneda-Almendra pegmatitic field (Central-Iberian Zone, Spain and Portugal). *Am. Mineral.* **2011**, *96*, 637–645. [[CrossRef](#)]
78. Roda-Robles, E.; Vieira, R.; Lima, A.; Errandonea-Martin, J.; Pesquera, A.; Cardoso-Fernandes, J.; Garate-Olave, I. Li-rich pegmatites and related peraluminous granites of the Fregeneda-Almendra field (Spain-Portugal): A case study of magmatic signature for Li enrichment. *Lithos* **2023**, *452–453*, 107195. [[CrossRef](#)]
79. Garate-Olave, I.; Roda-Robles, E.; Gil-Crespo, P.P.; Pesquera, A.; Errandonea-Martin, J. The Tres Arroyos Granitic Aplite-Pegmatite Field (Central Iberian Zone, Spain): Petrogenetic Constraints from Evolution of Nb-Ta-Sn Oxides, Whole-Rock Geochemistry and U-Pb Geochronology. *Minerals* **2020**, *10*, 1008. [[CrossRef](#)]
80. Keller, P.; Von Knorring, O. Pegmatites at the Okatjimukuju farm, Karibib, Namibia Part I: Phosphate mineral associations of the Clementine II pegmatite. *Eur. J. Mineral.* **1989**, *1*, 567–593. [[CrossRef](#)]
81. Baijot, M.; Hatert, F.; Philippo, S. Mineralogy and geochemistry of phosphates and silicates in the Sapucaia pegmatite, Minas Gerais, Brazil: Genetic implications. *Can. Mineral.* **2012**, *50*, 1531–1554. [[CrossRef](#)]
82. Vignola, P.; Zucali, M.; Rotiroti, N.; Marotta, G.; Risplendente, A.; Pavese, A.; Boscardin, M.; Mattioli, V.; Bertoldi, G. The chrysoberyl- and phosphate-bearing albite pegmatite of Malga Garbella Val Di Rabbi, Trento province, Italy. *Can. Mineral.* **2018**, *56*, 411–424. [[CrossRef](#)]
83. Roda-Robles, E.; Gil-Crespo, P.P.; Pesquera, A.; Lima, A.; Garate-Olave, I.; Merino-Martínez, E.; Cardoso-Fernandes, J.; Errandonea-Martin, J. Compositional Variations in Apatite and Petrogenetic Significance: Examples from Peraluminous Granites and Related Pegmatites and Hydrothermal Veins from the Central Iberian Zone (Spain and Portugal). *Minerals* **2022**, *12*, 1401. [[CrossRef](#)]
84. Piccoli, P.; Candela, P. Apatite in Igneous Systems. *Rev. Mineral.* **2002**, *48*, 255–292. [[CrossRef](#)]
85. Van Lichtervelde, M.; Linnen, R.L.; Salvi, S.; Beziat, D. The role of metagabbro rafts on tantalum mineralization in the Tanco pegmatite, Manitoba. *Can. Mineral.* **2006**, *44*, 625–644. [[CrossRef](#)]
86. London, D.; Morgan Vi, G.B.; Wolf, M.B. Amblygonite-montebasite solid solutions as monitors of fluorine in evolved granitic and pegmatitic melts. *Am. Mineral.* **2001**, *86*, 225–233. [[CrossRef](#)]
87. Kaeter, D.; Barros, R.; Menuge, J.F.; Chew, D.M. The magmatic hydrothermal transition in rare-element pegmatites from southeast Ireland: LA-ICP-MS chemical mapping of muscovite and columbite-tantalite. *Geochim. Cosmochim. Acta* **2018**, *240*, 96–130. [[CrossRef](#)]
88. Ballouard, C.; Elburg, M.A.; Tappe, S.; Reinke, C.; Ueckermann, H.; Doggart, S. Magmatic-hydrothermal evolution of rare metal pegmatites from the Mesoproterozoic Orange River pegmatite belt (Namaqualand, South Africa). *Ore Geol. Rev.* **2020**, *116*, 103252. [[CrossRef](#)]
89. Hulsbosch, N.; Muchez, P. Tracing fluid saturation during pegmatite differentiation by studying the fluid inclusion evolution and multiphase cassiterite mineralisation of the Gatumba pegmatite dyke system (NW Rwanda). *Lithos* **2020**, *354–355*, 105285. [[CrossRef](#)]
90. Shaw, R.A.; Goodenough, K.M.; Deady, E.; Nex, P.; Ruzvidzo, B.; Rushton, J.C.; Mounteney, I. The Magmatic–Hydrothermal Transition in Lithium Pegmatites: Petrographic and Geochemical Characteristics of Pegmatites from the Kamativi Area, Zimbabwe. *Can. Mineral.* **2022**, *60*, 957–987. [[CrossRef](#)]

91. Candela, P.A. A Review of Shallow, Ore-related Granites: Textures, Volatiles, and Ore Metals. *J. Petrol.* **1997**, *38*, 1619–1633. [[CrossRef](#)]
92. Thomas, R.; Davidson, P. Water in granite and pegmatite-forming melts. *Ore Geol. Rev.* **2012**, *46*, 32–46. [[CrossRef](#)]
93. Thomas, R.; Davidson, P. Revisiting complete miscibility between silicate melts and hydrous fluids, and the extreme enrichment of some elements in the supercritical state—Consequences for the formation of pegmatites and ore deposits. *Ore Geol. Rev.* **2016**, *72*, 1088–1101. [[CrossRef](#)]
94. Selway, J.B.; Breaks, F.W.; Tindle, A.G. A Review of Rare-Element (Li-Cs-Ta) Pegmatite Exploration Techniques for the Superior Province, Canada, and Large Worldwide Tantalum Deposits. *Explor. Min. Geol.* **2005**, *14*, 1–30. [[CrossRef](#)]
95. Martins, T.; Linnen, R.L.; Fedikow, M.A.F.; Singh, J. Whole-rock and mineral geochemistry as exploration tools for rare-element pegmatite in Manitoba: Examples from the Cat Lake–Winnipeg River and Wekusko Lake pegmatite fields (parts of NTS 52L6, 63J13). In *Report of Activities 2017*; Manitoba Growth, Enterprise and Trade, Manitoba Geological Survey: Winnipeg, MB, Canada, 2017; pp. 42–51.
96. Webber, K.L.; Falster, A.U.; Simmons, W.B.; Foord, E.E. The role of diffusion-controlled oscillatory nucleation in the formation of line rock in pegmatite-aplite dikes. *J. Petrol.* **1997**, *38*, 1777–1791. [[CrossRef](#)]
97. Webber, K.L.; Simmons, W.B.; Falster, A.U.; Foord, E.E. Cooling rates and crystallization dynamics of shallow level pegmatite-aplite dikes, San Diego County, California. *Am. Mineral.* **1999**, *84*, 708–717. [[CrossRef](#)]
98. Sirbescu, M.-L.C.; Hartwick, E.E.; Student, J.J. Rapid crystallization of the Animikie Red Ace Pegmatite, Florence county, northeastern Wisconsin: Inclusion microthermometry and conductive-cooling modeling. *Contrib. Mineral. Petrol.* **2008**, *156*, 289–305. [[CrossRef](#)]
99. Nabelek, P.I.; Whittington, A.G.; Sirbescu, M.-L.C. The role of H<sub>2</sub>O in rapid emplacement and crystallization of granite pegmatites: Resolving the paradox of large crystals in highly undercooled melts. *Contrib. Mineral. Petrol.* **2010**, *160*, 313–325. [[CrossRef](#)]
100. Pollard, P.J.; Pichavant, M.; Charoy, B. Contrasting evolution of fluorine- and boron-rich tin systems. *Mineral. Depos.* **1987**, *22*, 315–321. [[CrossRef](#)]
101. Thomas, R.; Webster, J.D.; Heinrich, W. Melt inclusions in pegmatite quartz: Complete miscibility between silicate melts and hydrous fluids at low pressure. *Contrib. Mineral. Petrol.* **2000**, *139*, 394–401. [[CrossRef](#)]
102. Thomas, R.; Förster, H.-J.; Heinrich, W. The behaviour of boron in a peraluminous granite–pegmatite system and associated hydrothermal solutions: A melt and fluid inclusion study. *Contrib. Mineral. Petrol.* **2003**, *144*, 457–472. [[CrossRef](#)]
103. Migdisov, A.A.; Williams-Jones, A.E. Hydrothermal transport and deposition of the rare earth elements by fluorine-bearing aqueous liquids. *Mineral. Depos.* **2014**, *49*, 987–997. [[CrossRef](#)]

**Disclaimer/Publisher’s Note:** The statements, opinions and data contained in all publications are solely those of the individual author(s) and contributor(s) and not of MDPI and/or the editor(s). MDPI and/or the editor(s) disclaim responsibility for any injury to people or property resulting from any ideas, methods, instructions or products referred to in the content.